CANCER

ATM-phosphorylated SPOP contributes to 53BP1 exclusion from chromatin during DNA replication

Dejie Wang[1,2†], Jian Ma[3,4†], Maria Victoria Botuyan[1†], Gaofeng Cui[1], Yuqian Yan[1], Donglin Ding[1], Yingke Zhou[1], Eugene W. Krueger[1], Jiang Pei[5], Xiaosheng Wu[6], Liguo Wang[7], Huadong Pei[8,9], Mark A. McNiven[1,10], Dingwei Ye[3,4]*, Georges Mer[1,10,11]*, Haojie Huang[1,10,12]*

53BP1 activates nonhomologous end joining (NHEJ) and inhibits homologous recombination (HR) repair of DNA double-strand breaks (DSBs). Dissociation of 53BP1 from DSBs and consequent activation of HR, a less error-prone pathway than NHEJ, helps maintain genome integrity during DNA replication; however, the underlying mechanisms are not fully understood. Here, we demonstrate that E3 ubiquitin ligase SPOP promotes HR during S phase of the cell cycle by excluding 53BP1 from DSBs. In response to DNA damage, ATM kinase–catalyzed phosphorylation of SPOP causes a conformational change in SPOP, revealed by x-ray crystal structures, that stabilizes its interaction with 53BP1. 53BP1-bound SPOP induces polyubiquitination of 53BP1, eliciting 53BP1 extraction from chromatin by a valosin-containing protein/p97 segregase complex. Our work shows that SPOP facilitates HR repair over NHEJ during DNA replication by contributing to 53BP1 removal from chromatin. Cancer-derived SPOP mutations block SPOP interaction with 53BP1, inducing HR defects and chromosomal instability.

INTRODUCTION

DNA double-strand breaks (DSBs) are deleterious DNA lesions that have been linked to chromosomal translocations and cancer. DSBs are repaired through the two main pathways of nonhomologous end joining (NHEJ) and homologous recombination (HR) (*1*). The DNA damage response (DDR) protein 53BP1 (*2*) regulates these DSB repair pathways. 53BP1 (p53-binding protein 1) promotes NHEJ by facilitating the long-range joining of broken DNA ends (*3*), while it antagonizes HR by inhibiting DNA end resection that generates 3′ single-stranded DNA (ssDNA) overhangs necessary for the search of homologous templates (*4*, *5*). Dependent on the ATM-H2AX-NBS1-MDC1-RNF8-RNF168 DSB signaling axis, 53BP1 localizes to chromatin by binding dimethylated lysine-20 on histone H4 (H4K20me2) and monoubiquitinated lysine-15 on histone H2A (H2AK15ub) through its tandem Tudor domain and ubiquitination-dependent recruitment (UDR) motif, respectively (*6*, *7*). At DSBs, 53BP1 suppresses DNA end resection through interaction with PTIP and RIF1, with RIF1 recruiting to break sites the ssDNA-binding shieldin complex (REV7, SHLD1, SHLD2, and SHLD3) that protects ssDNA from degradation by end-resection nucleases (*8*–*13*).

Extensive effort has been focused on understanding how the chromatin recruitment of 53BP1 in response to DSBs is facilitated or prevented. Many regulatory mechanisms have been uncovered, which include chromatin extraction or degradation of L3MBTL1, JMJD2A, and MBTD1, three proteins that compete with 53BP1 for binding H4K20me2 (*14*–*16*); TIP60-mediated acetylation of histone H4 at lysine-16 (H4K16ac) and H2A lysine-15 (H2AK15ac), two posttranslational modifications that inhibit the association of 53BP1 with chromatin (*17*, *18*); and direct interaction of 53BP1 tandem Tudor domain with TIRR, which blocks the H4K20me2 binding surface of 53BP1 (*19*, *20*). These different mechanisms have implications for DNA repair pathway selection, HR versus NHEJ, before 53BP1 recruitment to chromatin. A switch from error-prone NHEJ to the more accurate HR pathway occurs in chromatin-bound 53BP1 during DNA replication when sister chromatids direct the repair process. As cells transition through S phase of the cell cycle, dilution of H4K20me2 contributes to the reduction of 53BP1 foci in postreplicative chromatin (*21*). In parallel, BRCA1 interacts with H4K20me0 via its obligate partner BARD1 and is thereby recruited to postreplicative chromatin (*5*, *22*). Additional mechanisms controlling the removal of 53BP1 from chromatin must exist given that a large portion of H4K20me2 remains in S phase.

The *SPOP* gene is frequently mutated in human cancers such as prostate and endometrial cancers (*23*, *24*). It encodes a substrate-binding adaptor of the Cullin3 (CUL3)–RING-box 1 (RBX1) E3 ubiquitin ligase (CRL) complex. Biochemical and mouse genetic studies have identified a number of prostate cancer–relevant proteins as the degradation substrates of SPOP, such as androgen receptor, BMI1, SRC3, TRIM24, and BRD4 (*25*–*28*). Speckle-type POZ protein (SPOP) is also implicated in regulating genomic stability (*29*–*31*); however, how SPOP controls genomic stability is unclear. In the present study, we show that SPOP functions as an E3 ubiquitin ligase that binds to 53BP1 primarily during S phase and catalyzes K29-linked polyubiquitination of 53BP1. SPOP-dependent 53BP1 polyubiquitination triggers the eviction of 53BP1 from chromatin,

[1]Department of Biochemistry and Molecular Biology, Mayo Clinic College of Medicine and Science, Rochester, MN 55905, USA. [2]Department of Gastroenterology, Collaborative Innovation Center of Gastroenterology, Angiocardiopathy and Neurosciences, The First Affiliated Hospital of Nanchang University, Nanchang, Jiangxi 330006, China. [3]Department of Urology, Fudan University Shanghai Cancer Center, Shanghai 200032, China. [4]Department of Oncology, Shanghai Medical College, Fudan University, Shanghai 200032, China. [5]State Key Laboratory of Proteomics, National Center for Protein Sciences, Beijing Institute of Lifeomics, Beijing 102206, China. [6]Division of Hematology, Mayo Clinic College of Medicine and Science, Rochester, MN 55905, USA. [7]Division of Computational Biology, Mayo Clinic College of Medicine and Science, Rochester, MN 55905, USA. [8]George Washington University Cancer Center, Washington, DC 20037, USA. [9]Department of Biochemistry and Molecular Medicine, George Washington University School of Medicine and Health Science, Washington, DC 20037, USA. [10]Mayo Clinic Cancer Center, Mayo Clinic College of Medicine and Science, Rochester, MN 55905, USA. [11]Department of Cancer Biology, Mayo Clinic College of Medicine and Science, Rochester, MN 55905, USA. [12]Department of Urology, Mayo Clinic College of Medicine and Science, Rochester, MN 55905, USA.
*Corresponding author. Email: huang.haojie@mayo.edu (H.H.); mer.georges@mayo.edu (G.M.); dingwei_ye1963@163.com (D.Y.)
†These authors contributed equally to this work.

which promotes DNA repair by HR over NHEJ. We demonstrate "post commitment" selection of HR over NHEJ in the context of chromatin-engaged 53BP1.

RESULTS

SPOP recognizes the focus-forming region of 53BP1

To determine how SPOP regulates DNA repair, we examined whether SPOP F133V, one of the most frequent SPOP mutants in patients with prostate cancer, would affect the expression of several NHEJ and HR pathway proteins. SPOP F133V did not appreciably change the expression of these proteins in prostate cancer cell line PC-3 and benign prostate cell line BPH1, whether the cells were exposed to ionizing radiation (IR) (Fig. 1A). Similar results were obtained in SPOP knockdown cells, but with a moderate decrease in expression of RAD51 HR recombinase (fig. S1A). These observations agree well with studies done in other prostate cancer cell lines (*31*). We further explored the influence of SPOP F133V on the repair pathway choice using various methods including reporter genes, 53BP1 IR-induced foci (IRIF) formation and live cell imaging. Different from the effect of SPOP wild type (WT), expression of SPOP F133V mutant or SPOP knockout (KO) inhibited HR, increased NHEJ, and prolonged 53BP1 retention at DNA damage sites (Fig. 1, B to G, and fig. S1, B to N), suggesting that SPOP controls 53BP1 retention in chromatin at DSB sites. Consistent with this hypothesis, ectopically expressed SPOP bound to 53BP1 but not to the other DNA repair proteins that we examined (Fig. 1H and fig. S1O) and colocalized with 53BP1 and γ-H2AX foci after IR treatment (fig. S1P). The SPOP-53BP1 interaction was confirmed at the endogenous level in different cell lines (Fig. 1I and fig. S1Q) and was markedly enhanced after induction of DNA damage by IR or camptothecin (CPT) (Fig. 1, H and I, and fig. S1, O, Q, and R).

To define which region in 53BP1 mediates its interaction with SPOP, we transfected 293T cells with a series of plasmids expressing hemagglutinin (HA)–tagged C-terminally truncated mutants of 53BP1. Coimmunoprecipitation (co-IP) assays demonstrated that the focus-forming region (FFR; residues 1220 to 1712) was required for 53BP1 binding to SPOP (Fig. 1, J and K). 53BP1 FFR directly bound to SPOP in vitro (Fig. 1L). Therefore, 53BP1 FFR is necessary and sufficient for direct binding of 53BP1 to SPOP.

Structural basis for the interaction of 53BP1 with SPOP

SPOP harbors an N-terminal MATH domain that recognizes a SPOP-binding consensus sequence (SBC; Φ-π-S-S/T-S/T where Φ is a nonpolar residue and π is a polar residue) in SPOP client proteins (*32*). There are two putative SBCs in the FFR region of 53BP1, ^{1313}HRTSS^{1317} and ^{1641}ASSSS^{1645}, of which only deletion of the latter diminished the SPOP-53BP1 interaction (Fig. 1, M to O). We next used nuclear magnetic resonance (NMR) spectroscopy to precisely identify the SPOP-binding region of 53BP1. We expressed in *Escherichia coli* a segment of human 53BP1 from residues 1606 to 1656 (53BP1$^{1606–1656}$) and assigned the associated ^{1}H, ^{15}N, and ^{13}C backbone resonance signals (Fig. 2A). From the ^{1}Hα, ^{1}HN, ^{13}Cα, ^{13}Cβ, ^{13}CO, and ^{15}N chemical shift values (*33*), we determined that 53BP1$^{1606–1656}$ is entirely disordered. Upon addition of unlabeled SPOP MATH domain to ^{15}N-labeled 53BP1$^{1606–1656}$, there was signal broadening in the ^{1}H-^{15}N heteronuclear single quantum coherence (HSQC) spectra from residues S1635 to T1648 (Fig. 2B), indicating that this region of 53BP1 is in contact with SPOP. Deletion of ^{1635}SPATPTASSSSSTT^{1648} completely disrupted the basal level interaction between SPOP and 53BP1 and also blocked the DNA damage–enhanced interaction (Fig. 1, M and O). We have therefore identified a functional SPOP binding motif (SBM; residues 1635 to 1648) in FFR that is required for the interaction of 53BP1 with SPOP. We note that the SBM is adjacent to the UDR (residues 1611 to 1631) of 53BP1 (Fig. 1M). We also used NMR spectroscopy to map the 53BP1-binding site on the surface of SPOP. The ^{1}H-^{15}N HSQC NMR spectra of ^{15}N-labeled SPOP MATH domain titrated with unlabeled 53BP1$^{1606–1656}$ showed chemical shift perturbations consistent with the peptide binding area detected in other structures of SPOP-peptide complexes (*32*, *34*, *35*), including Y87, W131, F133, and K134 (Fig. 2, C and D).

To understand how SPOP recognizes 53BP1, we determined x-ray crystal structures of SPOP MATH domain in the apo state and bound to a 53BP1 SBM peptide (residues 1636 to 1650) at resolutions of 1.48 and 1.44 Å, respectively. The structural statistics are reported in table S1. In agreement with the solution NMR spectroscopy data, 53BP1 interacts with a shallow cavity in SPOP composed mainly of residues R70, Y87, F102, M117, Y123, K129, D130, W131, G132, and F133. Eight 53BP1 residues (T1638 to S1645) could be modeled in the electron density map (Fig. 2, D and E, and fig. S2A). The hydrophobic side chain of 53BP1 A1641 (Φ in the SBC motif) is surrounded by the aromatic side chains of SPOP F102, Y123, W131, and F133. The carbonyl and hydroxyl groups of A1641 and Y123, respectively, are connected via hydrogen bonds mediated by a water molecule. 53BP1 S1642 (π in the SBC motif) is close in space to Y87, W131, and G132 of SPOP, with the amide and carbonyl groups of S1642 forming hydrogen bonds with the carbonyl and amide groups of G132. There is an extensive network of polar interactions at the SPOP-53BP1 interface involving four 53BP1 serine residues. The hydroxyl groups of S1642 and SPOP Y87 and the carbonyl of S1643 are bridged by three water-mediated hydrogen bonds. The hydroxyl group of S1643 forms hydrogen bonds with the carbonyl and carboxylate groups of SPOP D130. The amide group of S1644 is hydrogen-bonded to the carboxylate group of SPOP D130, while the hydroxyl group of S1644 forms hydrogen bonds with the carboxylate and guanidinium groups of SPOP D130 and R70, respectively. The carbonyl and hydroxyl groups of S1645 are hydrogen-bonded to SPOP K129. 53BP1 P1639 is in contact with SPOP M117.

SPOP promotes lysine-29–linked 53BP1 polyubiquitination and prostate cancer–derived SPOP mutants impair this process and enhance 53BP1 retention at DSB sites

SPOP being an E3 ubiquitin ligase, substrate-binding MATH domain (ΔMATH), and CUL3-binding BTB (ΔBTB) deletion mutants are nonfunctional for substrate ubiquitination. Ectopic expression of WT SPOP as well as ΔMATH and ΔBTB did not affect the steady-state level of 53BP1 in 293T cells (fig. S2C), indicating that SPOP does not regulate ubiquitin-dependent degradation of 53BP1. Notably, SPOP expression induced a marked increase in 53BP1 polyubiquitination upon DNA damage after IR treatment (fig. S2D). KO of endogenous SPOP by CRISPR-Cas9 greatly attenuated 53BP1 polyubiquitination, and this was reversed by restored expression of SPOP (fig. S2D), indicating that SPOP contributes to 53BP1 polyubiquitination. CPT treatment enhanced SPOP-induced polyubiquitination of 53BP1 (fig. S2E). SPOP specifically augmented K29-linked polyubiquitination of 53BP1 in cells under a DNA-damaging condition (fig. S2, F and G). SPOP expression also increased 53BP1

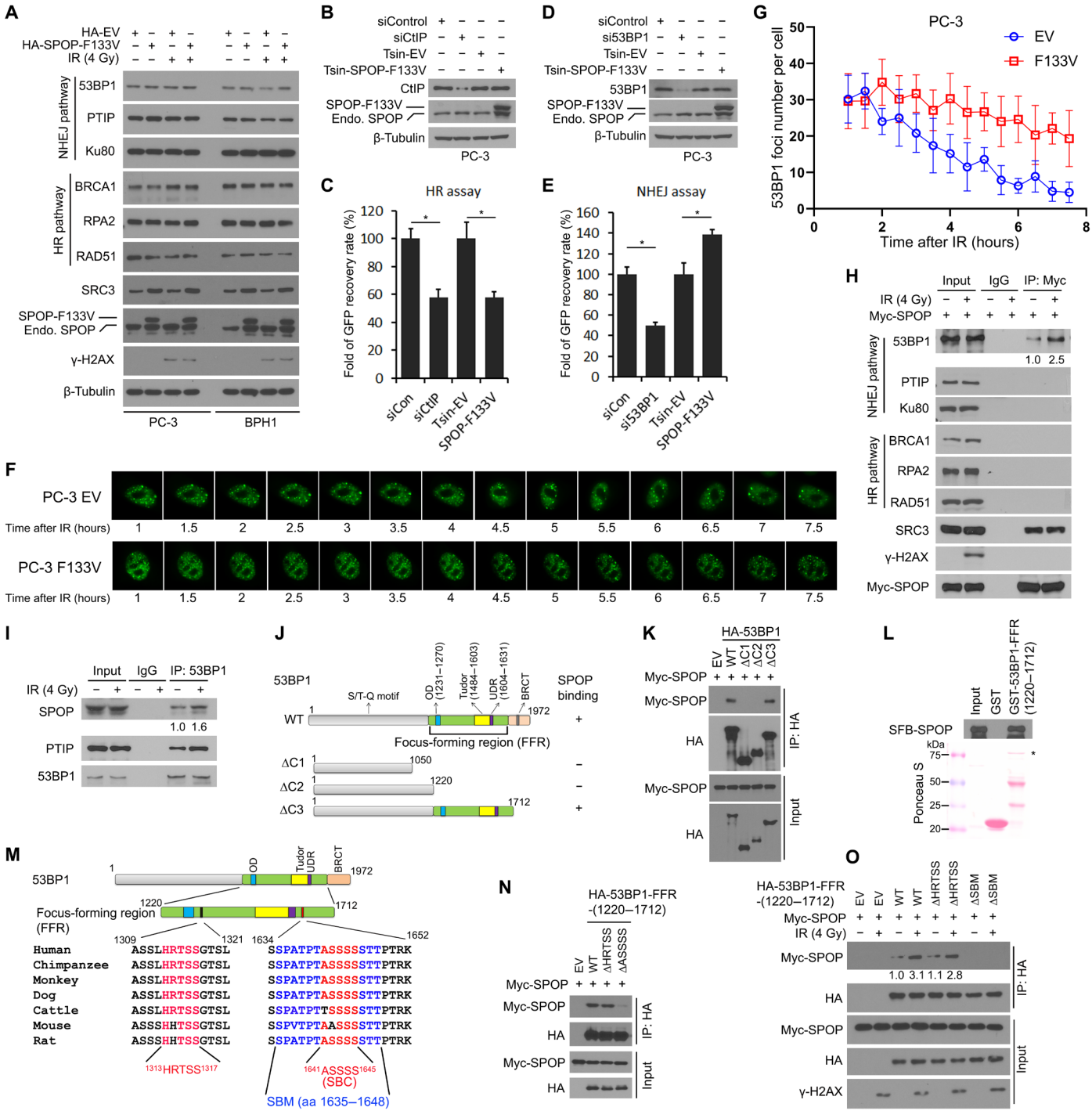

Fig. 1. SPOP binds a specific motif in 53BP1. (**A**) Western blot (WB) of DDR proteins in PC-3 and BPH1 cells transfected with empty vector (EV) or SPOP F133V mutant and/or treated with or without IR for 1 hour. SRC3, a known SPOP substrate. Endo., endogenous. HA, hemagglutinin. (**B** to **E**) PC-3 cells were transfected with HR or NHEJ reporter in combination with SPOP F133V or small interfering RNA (siRNA) for CtIP or 53BP1 followed by WB (B and D) and HR and NHEJ activity measurement (C and E). Data are represented as means ± SD of three biological replicates. *$P < 0.05$. GFP, green fluorescent protein. (**F** and **G**) Live cell imaging (F) and quantification (G) of GFP-53BP1 foci in PC-3 cells transfected with EV or SPOP F133V at indicated time points after IR (4 Gy). Data are represented as means ± SD of 10 live cells. (**H** and **I**) PC-3 cells either transfected with Myc-SPOP (H) or untransfected (I) were treated with IR for 1 hour followed by coimmunoprecipitation (co-IP) and WB. (**J**) Schematic of 53BP1 domain structure and constructs. IgG, immunoglobulin G. (**K**) 293T cells transfected with indicated constructs were treated with IR for 1 hour and harvested for co-IP and WB. (**L**) Glutathione *S*-transferase (GST) pull-down assay using in vitro transcribed and translated SFB-SPOP protein and GST-tagged recombinant proteins. Asterisk, the expected protein. (**M**) Diagram showing two putative SPOP-binding consensus motifs (in pink and red) in 53BP1-FFR. aa, amino acids. (**N** and **O**) 293T cells transfected with indicated constructs were treated with IR for 1 hour followed by co-IP and WB.

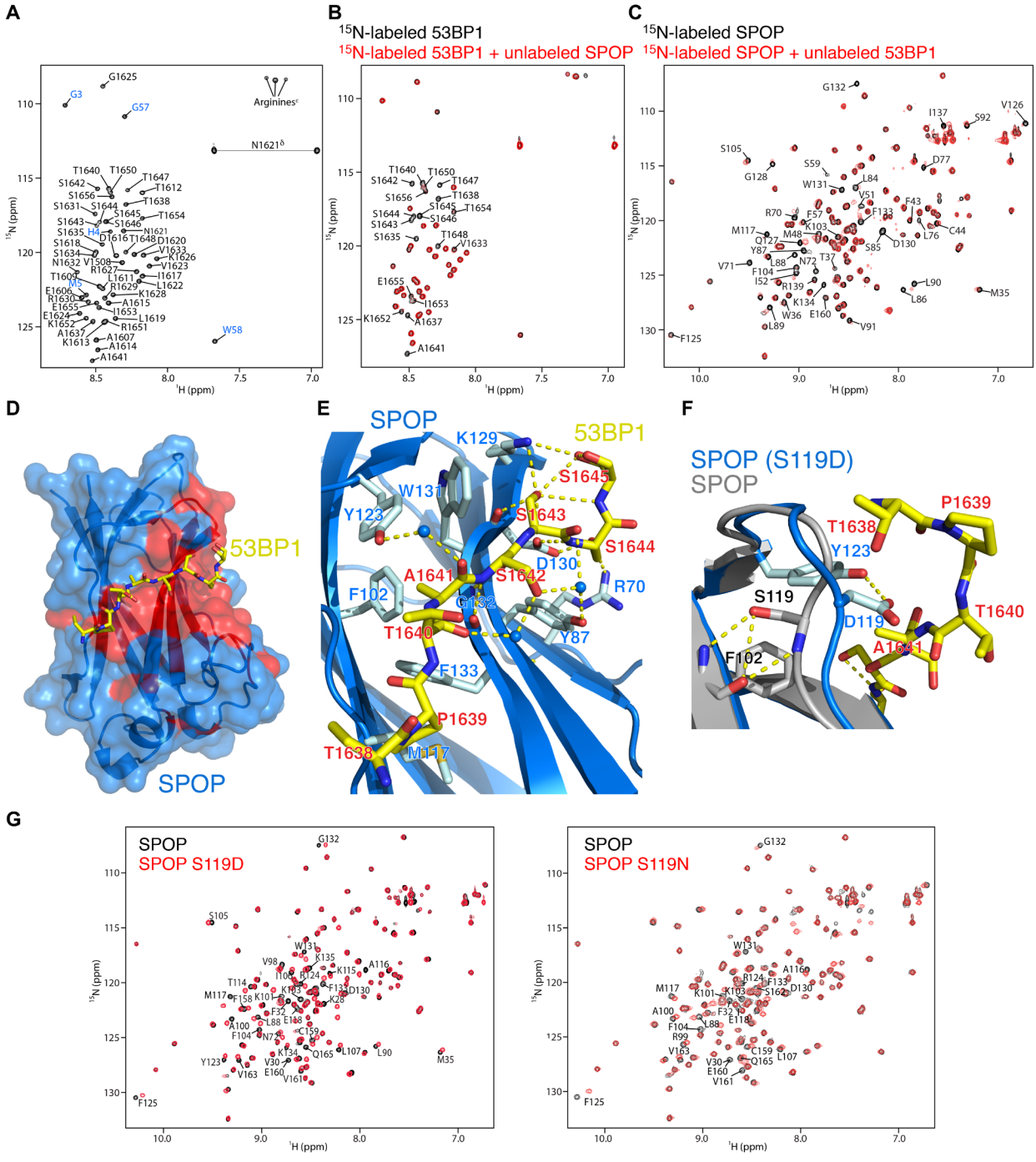

Fig. 2. Structural basis for the interaction of 53BP1 with SPOP and SPOP phosphorylated at serine-119. (**A**) Backbone NMR signal assignments of 53BP1$^{1606–1656}$. Shown is the ^{1}H-^{15}N heteronuclear single quantum coherence (HSQC) spectrum of ^{15}N- and ^{13}C-labeled 53BP1 (residues 1606 to 1656) with assigned signals. In blue are residues remaining from the expression plasmid (G3, H4, and M5) and two C-terminal residues (G57 and W58) added for protein quantification by ultraviolet light absorption. (**B**) Representative ^{1}H-^{15}N HSQC spectra of the interaction of ^{15}N-labeled 53BP1 (residues 1606 to 1656) with unlabeled SPOP MATH domain. The 53BP1:SPOP molar ratio is 1:2. The spectra were recorded at 4°C. (**C**) Representative ^{1}H-^{15}N HSQC spectra of the interaction of ^{15}N-labeled SPOP MATH domain with nonlabeled 53BP1 (residues 1606 to 1656). The SPOP:53BP1 molar ratio is 1:6. The spectra were recorded at 25°C. (**D**) Surface and cartoon representation of the x-ray crystal structure of the SPOP MATH domain in complex with a 53BP1 SBM synthetic peptide (residues 1636 to 1650). SPOP residues for which NMR signals are affected by 53BP1 binding (see C) are highlighted in red. (**E**) Details of the SPOP-53BP1 interface in the crystal structure. The blue spheres represent water molecules. The yellow dashes represent hydrogen bonds. (**F**) Comparison of the SPOP-53BP1 and SPOP S119D-53BP1 crystal structures highlighting the change in conformation in SPOP S119D that brings D119 in contact with 53BP1. SPOP WT and S119D are shown in gray and blue, respectively. Key residues in the vicinity of S119 and D119 in the two structures are labeled. Hydrogen bonds involving S119 and D119 are shown as yellow dashes. (**G**) Effects of S119D and S119N mutations on SPOP structure. Shown are the ^{1}H-^{15}N HSQC spectra of SPOP MATH mutants S119D and S119N overlaid to that of WT SPOP MATH.

FFR polyubiquitination, and this effect was enhanced by CPT treatment (fig. S2H). However, SBM deletion abolished SPOP-mediated polyubiquitination of 53BP1 FFR in cells in the presence or absence of DNA damage and prolonged 53BP1 retention at DNA damage sites (fig. S2, H and I). Therefore, SPOP binding to SBM promotes K29-linked polyubiquitination of 53BP1.

Similar to SPOP ΔMATH, eight SPOP MATH domain mutants frequently detected in prostate cancer—Y87C, F102C, S119N, F125V, K129E, W131G, F133V, and F133L (*36*)—failed to interact with 53BP1 even in cells exposed to IR (fig. S2, J to L). Like SPOP ΔMATH or ΔBTB, which are nonfunctional for ubiquitination, the patient-derived SPOP mutants also failed to promote 53BP1 polyubiquitination even after IR treatment (fig. S2, M and N). Expression of these mutants had little or no influence on 53BP1 protein level in 293T cells (fig. S2O).

Most of the SPOP mutants detected so far are hemizygous, and they act in a dominant negative fashion (*23*, *28*, *36*, *37*). To recapitulate the pathophysiological conditions of patients, we introduced the mutated allele of SPOP into prostate cancer cell lines PC-3 and U2OS (a cell model commonly used for IRIF analysis) that do not harbor any endogenous SPOP mutant. While introduction of SPOP hotspot mutants F102C and F133V into PC-3 and U2OS cells had no impact on the recruitment of 53BP1 at 1 hour after IR, their expression prolonged 53BP1 retention at 4 to 8 hours after IR (fig. S3, A to G). Thus, prostate cancer–derived SPOP mutations impair the SPOP-53BP1 interaction and 53BP1 polyubiquitination and promote 53BP1 retention at DSB sites.

We also examined whether SPOP affects the roles of 53BP1 in class switch recombination (CSR), inhibition of HR in BRCA1-deficient cells, and checkpoint/p53 function. We found that while, as expected, 53 bp1 KO inhibited the CSR in CH12F3-C2 murine B cells (*38*), Spop KO had no effect on CSR in the presence or absence of 53 bp1 deletion (fig. S3, H to J), suggesting that SPOP does not affect 53BP1 regulation of CSR. As expected, 53BP1 KO induced HR in BRCA1-deficient U2OS-DR cells (*39*). Expression of SPOP WT also increased HR in these cells, but no further increase was observed in 53BP1 KO cells (fig. S3, K and L), suggesting that SPOP and 53BP1 regulate HR through the same pathway. Similar to the results reported previously (*40*), 53BP1 KO decreased p21 expression and increased cell number in S phase in U2OS cells in response to DNA damage (fig. S3, M and N). Expression of SPOP F133V mutant resulted in a greater reduction in p21 expression and higher induction of cells in S phase compared with 53BP1 KO, and similar results were obtained in cells expressing both sg53BP1 and SPOP F133V (fig. S3, M and N). These data indicate that the effect of SPOP mutation on cell cycle checkpoint/p53 function is very complex and that it could be mediated through 53BP1-dependent and 53BP1-independent mechanisms.

Phosphorylation of SPOP serine-119 by ATM kinase augments SPOP-mediated 53BP1 polyubiquitination and 53BP1 retention at DSB sites

Several protein kinases are activated in response to DNA damage and mediate DNA repair signaling by phosphorylating target proteins. To determine whether phosphorylation contributes to DNA damage–enhanced SPOP-53BP1 interaction and 53BP1 polyubiquitination, we used cell lysates treated or not with λ protein phosphatase in pull-down assays with recombinant glutathione *S*-transferase–53BP1 FFR purified from *E. coli*. Phosphatase treatment abolished DNA damage–enhanced SPOP-53BP1 interaction (Fig. 3A), suggesting that phosphorylation of SPOP is important for optimal interaction with 53BP1 under DNA damage conditions.

To define which kinases mediate SPOP phosphorylation in response to DNA damage, we exposed 293T cells to IR and subsequently treated them with small-molecule inhibitors specific for kinases involved in the DDR or cell cycle regulation. Only ATM kinase inhibitor treatment attenuated the SPOP-53BP1 interaction in IR-treated cells (Fig. 3B). Reciprocal co-IP assays showed that SPOP interacts with ATM at the endogenous protein level in 293T cells (Fig. 3C). In in vitro kinase assays, SPOP was only phosphorylated by WT ATM but not the kinase-dead mutant purified from IR-treated cells (Fig. 3D). There are three serine/threonine-glutamine (S/T-Q) sites (T25-Q, S119-Q, and T319-Q) in SPOP that match the consensus phosphorylation sequence of ATM. Only the S119A mutation in the MATH domain, but not T25A or T319A, abolished ATM-mediated phosphorylation of SPOP in vitro (Fig. 3D). SPOP was phosphorylated by ATM in 293T cells treated with IR, but this effect was abolished by the S119A mutation (Fig. 3E). Our data indicate that ATM phosphorylates SPOP primarily at S119 in vitro and in cells.

Like λ phosphatase treatment (Fig. 3A), ATM knockdown decreased SPOP-53BP1 interaction in IR-treated 293T cells (Fig. 3F). Moreover, the phosphomimicking S119D and S119E mutants augmented SPOP-53BP1 interaction and 53BP1 polyubiquitination even in cells not exposed to IR (Fig. 3, G and H). In contrast, the phosphorylation-resistant S119A mutation of SPOP prevented IR-augmented SPOP-53BP1 interaction and blocked IR-enhanced polyubiquitination of 53BP1 (Fig. 3, G and H). Using x-ray crystallography (table S1) and NMR spectroscopy, we verified that the S119A mutation does not alter the three-dimensional (3D) structure of SPOP MATH, highlighting the key role of phosphorylation in enhancing 53BP1 polyubiquitination. Using in vitro ubiquitination assays, we showed that ATM enhanced WT SPOP-mediated polyubiquitination of 53BP1 FFR, but polyubiquitination was abrogated by the S119N mutation (Fig. 3I). SPOP S119N is a prostate cancer–associated mutant that, like S119A (Fig. 3G), diminishes the interaction of SPOP with 53BP1 in cells (fig. S2L). The S119A and S119N mutations significantly increased the number of 53BP1 IRIF at 4 and 8 hours after IR (Fig. 3, J to L). In contrast, phosphomimetic mutants S119D and S119E significantly reduced the number of 53BP1 IRIF at 4 hours after IR (Fig. 3, J to L). Our data show that ATM-mediated phosphorylation of SPOP at S119 enhances SPOP interaction with 53BP1 and 53BP1 polyubiquitination and decreases 53BP1 retention at DSB sites.

Structural basis for enhanced interaction of 53BP1 with serine-119–phosphorylated SPOP

To understand how phosphorylation of SPOP at S119 increases its interaction with 53BP1, we determined the x-ray crystal structure of SPOP MATH S119D phosphomimetic mutant in complex with 53BP1 SBM at 3.0-Å resolution (Fig. 2F, fig. S2B, and table S1). While SPOP S119 is stabilized by intramolecular hydrogen bonds with the amide and carbonyl groups of F102 and does not contact 53BP1 or any other SPOP-binding peptides characterized in complex with SPOP, the S119D mutation causes a marked local conformational change in SPOP that brings D119 in close proximity to 53BP1 (Fig. 2F). In the structure of SPOP S119D bound to 53BP1, the carboxylate group of D119 points toward 53BP1 and is in proximity of the amide groups of 53BP1 T1640 and A1641 and carbonyl groups of T1638 and T1640 (Fig. 2F). In addition, the carboxylate of

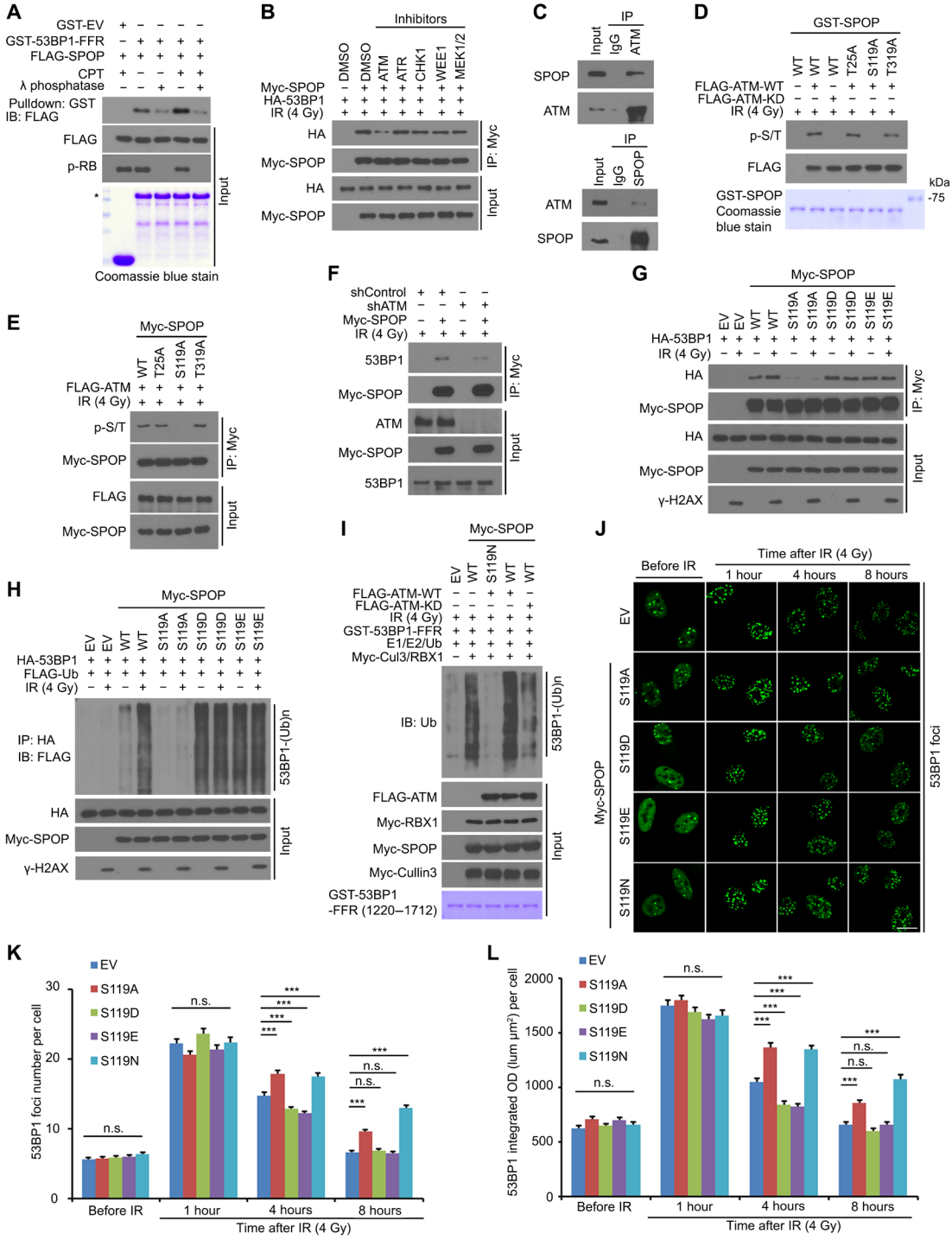

Fig. 3. Phosphorylation of SPOP by ATM kinase enhances its binding to 53BP1. (**A**) GST pulldown using λ phosphatase–treated lysate from 293T cells transfected with FLAG-SPOP. Asterisk, the GST-53BP1 FFR protein. Phosphorylated RB, monitoring phosphatase efficacy. IB, immunoblotting. (**B**) Co-IP and WB in 293T cells transfected with indicated plasmids and pretreated with inhibitors of kinases followed by IR treatment for 1 hour. DMSO, dimethyl sulfoxide; MEK1/2, mitogen-activated protein kinase kinase 1/2. (**C**) Reciprocal co-IP of endogenous ATM and SPOP in 293T cells 1 hour after IR. (**D**) 293T cells transfected with indicated constructs were treated with IR for 1 hour. Immunoprecipitated FLAG-ATM proteins were incubated with GST-SPOP proteins purified from *E. coli* for in vitro kinase assay followed by WB. (**E** and **F**) 293T cells were transfected with indicated plasmids and treated with IR for 1 hour followed by WB. (**G** and **H**) co-IP (G) or in vivo polyubiquitination assay (H) in 293T cells transfected with indicated plasmids and treated with IR (4 Gy) for 1 hour. (**I**) In vitro ubiquitination assay using the substrate GST-53BP1-FFR and indicated proteins immunoprecipitated from 293T cells treated with IR for 1 hour. (**J** to **L**) PC-3 cells transfected with indicated constructs were treated with IR followed by immunofluorescent cytochemistry (IFC) of 53BP1 at the indicated time points after IR (J). Scale bar, 10 μM. The average 53BP1 foci number (K) and foci density (L) in each cell were quantified. Data are presented as means ± SEM of more than 300 cells from three biological replicates. n.s., not significant, ***$P < 0.001$.

D119 is hydrogen-bonded to the hydroxyl group of SPOP Y123, which is also close in space to the carbonyl group of T1648. The SPOP (S119D)–53BP1 structure explains why an aspartate can mimic a phosphoserine. It is expected that like D119, a phosphoserine at position 119 would point toward 53BP1 and would strengthen the SPOP-53BP1 interaction even more in comparison to an aspartate. The hydroxyl group of T1638 points toward the carboxylate group of D119 and would likely be hydrogen-bonded to a phosphoserine at position 119 (Fig. 2F). The crystallography data suggest that in addition to the SBC segment of 53BP1 SBM (residues 1641 to 1645) that binds SPOP, SPOP S119 phosphorylation creates a new binding surface that is recognized by the N terminus of SBM (residues 1638 to 1640) (Fig. 2, E and F). No other known SPOP substrates recognize a phosphate group. This additional binding mode is supported by co-IP data showing that DNA damage only enhanced SPOP interaction with 53BP1 but not with other known substrates examined (fig. S3O). It is noteworthy that phospho-dependent protein-protein interactions usually involve recognition of a flexible phosphorylated protein segment (e.g., a phosphopeptide) by a well-ordered or folded receptor domain, for example, a BRCT domain (*41*). Here, phosphorylation is in the receptor domain (SPOP), not in the flexible motif (53BP1).

SPOP MATH S119D had slightly higher affinity for the 53BP1 peptide than WT SPOP MATH with respective dissociation constants (K_ds) of 42.5 ± 4.4 and 60.7 ± 8.1 μM determined using isothermal titration calorimetry (ITC) (fig. S3P). These K_d values are of the same order of magnitude as those measured for other SPOP-peptide interactions (*35*, *42*). While the difference in affinity is small, in the context of full-length proteins in cells, the effect of S119 phosphorylation may be amplified. Both SPOP MATH-BTB and 53BP1 FFR are dimeric proteins (*20*, *32*). It is expected that the two MATH domains in a SPOP dimer simultaneously bind the two SBMs in a 53BP1 dimer already bound to the nucleosome. The avidity effect of such multivalent interaction of SPOP and 53BP1 may result in an enhanced affinity difference in comparison to a monomeric MATH domain binding a short 53BP1 peptide. Furthermore, this effect may be further enhanced by protein autoassociations and phase separation in cells, processes in which SPOP (*43*) and 53BP1 (*44*) participate.

Thermal melt assays showed that with an estimated melting temperature (T_m) of 43°C, SPOP S119D MATH domain is less stable than WT SPOP MATH for which the T_m is estimated to be 50°C (fig. S3Q). The lower stability of SPOP S119D was expected as the conformational changed caused by this mutation (and presumably phosphorylation) disrupts hydrogen bonds involving the amide nitrogen atom and hydroxyl group of serine-119 with the carbonyl group and amide nitrogen atom of Phe^{102}, respectively (Fig. 2F).

Like S119D, the prostate cancer–associated S119N mutation likely causes a change in SPOP MATH conformation as suggested by NMR spectroscopy (Fig. 2G). While S119D (and S119 phosphorylation) facilitates SPOP binding to 53BP1, S119N markedly diminishes this interaction in cells. The conformational change in SPOP S119N must differ from that associated with S119D, which might explain differences in signal perturbations in the NMR spectra of S119D and S119N (Fig. 2G).

SPOP interacts with and mediates 53BP1 polyubiquitination primarily during S phase

A temporal analysis in different cell types revealed that 53BP1 IRIF were most prominent during G_1 phase of the cell cycle and progressively decreased in intensity when cells transited from early to late S phases (*5*). We sought to determine whether SPOP regulates 53BP1 polyubiquitination in a cell cycle–dependent manner using PC-3 cells synchronized by release from nocodazole treatment (Fig. 4A). In these cells, the level of SPOP protein expression varied during the cell cycle with the highest expression occurring in S phase (Fig. 4, A and B). Similar results were obtained in Hela cells (*45*). As we anticipated, SPOP predominantly interacted with 53BP1 in S-phase cells (Fig. 4, A and B), and the interaction was enhanced under DNA damage conditions (fig. S4A). In agreement with these observations, 53BP1 was highly polyubiquitinated in S-phase cells (Fig. 4, A and C). Subcellular fractionation assays showed that the level of chromatin-bound polyubiquitinated 53BP1 was decreased in SPOP WT-overexpressing cells compared to that of empty vector–expressing control cells (fig. S4B). Accordingly, we showed that expression of SPOP WT in PC-3 cells decreased retention of 53BP1 at DSB sites at 4 to 8 hours after IR (Fig. 4, D to F). In contrast, introduction of SPOP F102C and F133V, two hotspot mutants derived from patients with prostate cancer, largely impaired 53BP1 IRIF in S-phase cells at 4 to 8 hours after IR although their expression had no obvious effect on 53BP1 retention at DSB sites at 1 hour after IR (Fig. 4, D to F). Similar results were obtained in U2OS cells (fig. S4, C to E). These observations indicate that SPOP primarily interacts with and promotes 53BP1 polyubiquitination during S phase (Fig. 4, A and B).

SPOP regulates 53BP1 retention at DSB sites by controlling 53BP1 interaction with the valosin-containing protein/p97 cofactor NPL4

The adenosine triphosphatase valosin-containing protein (VCP/p97) segregase complex has been implicated in ubiquitin conjugation-dependent removal of DNA damage regulatory proteins from DSB sites (*15*, *46*). Because SPOP mutations significantly prolong 53BP1 retention at DSB sites (figs. S1, H to N, and S3, A to G), we asked whether 53BP1 is a SPOP-dependent target of VCP/p97. We first examined whether 53BP1 interacts with p97 and/or its cofactors. Co-IP assays showed that 53BP1 specifically interacted with NPL4, but not other cofactors of p97 in PC-3 and 293T cells and that their interaction was enhanced by SPOP (Fig. 5, A and B). However, none of the eight high-frequency prostate cancer–derived SPOP mutants could promote 53BP1-NPL4 interaction to a level approaching that of WT SPOP (Fig. 5C). These data suggest that SPOP-enhanced NPL4-53BP1 interaction is abolished by prostate cancer–derived SPOP mutations.

Next, we examined how SPOP-regulated 53BP1-NPL4 interaction affects 53BP1 occupancy at DSB sites. We could not completely knock out NPL4 in PC-3 cells but were able to significantly reduce endogenous NPL4 level (Fig. 5D). Decreased expression of NPL4 substantially delayed the initial recruitment of 53BP1 to DSB sites at 1 hour of IR exposure (Fig. 5, D to G). This is likely due to impaired NPL4-mediated removal of L3MBTL1 from DSBs because L3MBTL3 is an H4K20me2 reader that blocks 53BP1 recruitment (*15*). However, at longer time points after IR (4 and 8 hours), NPL4 depletion significantly prolonged the retention of 53BP1 IRIF compared to control sgRNA (single guide RNA) (sgControl) cells (Fig. 5, D to G), suggesting that NPL4 also influences 53BP1 retention at DSB sites. We made similar observations in cells expressing cancer-associated SPOP hotspot mutant F133V alone or in combination with NPL4 depletion at 4 to 8 hours after IR, but no such defect was detected in

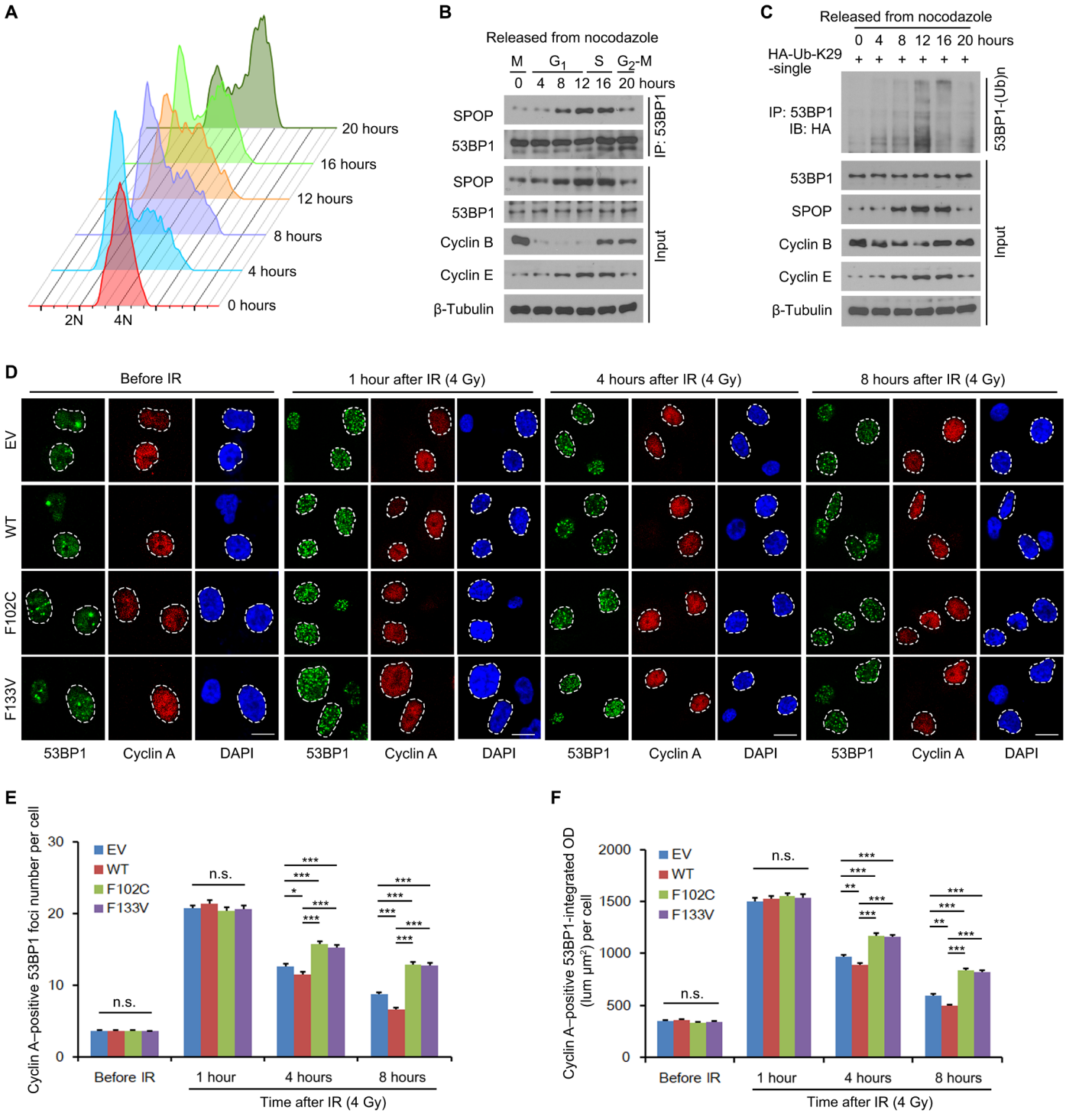

Fig. 4. SPOP interaction of 53BP1 and 53BP1 K29-linked polyubiquitination are elevated in the S phase. (**A** and **B**) PC-3 cells were synchronized with nocodazole (100 ng/ml) for 12 hours and released into the cell cycle. At the indicated time points, cells were harvested for cell cycle (A) and co-IP and WB analysis (B). (**C**) PC-3 cells were transfected with HA-Ub-K29 construct and released from nocodazole. Cells were harvested for IP at indicated time points. (**D** to **F**) PC-3 cells were infected with lentivirus expressing EV, SPOP WT, or mutants F102C and F133V. Representative 53BP1 foci in S-phase cells are shown (D). Cyclin A–positive staining indicated the cells are in S phase. The average 53BP1 foci number (E) and foci density (F) in S-phase cells were quantified. Scale bars, 10 μM. Data are presented as means ± SEM of more than 300 cells from three biological replicates. *$P < 0.05$, **$P < 0.01$, and ***$P < 0.001$. DAPI, 4′,6-diamidino-2-phenylindole.

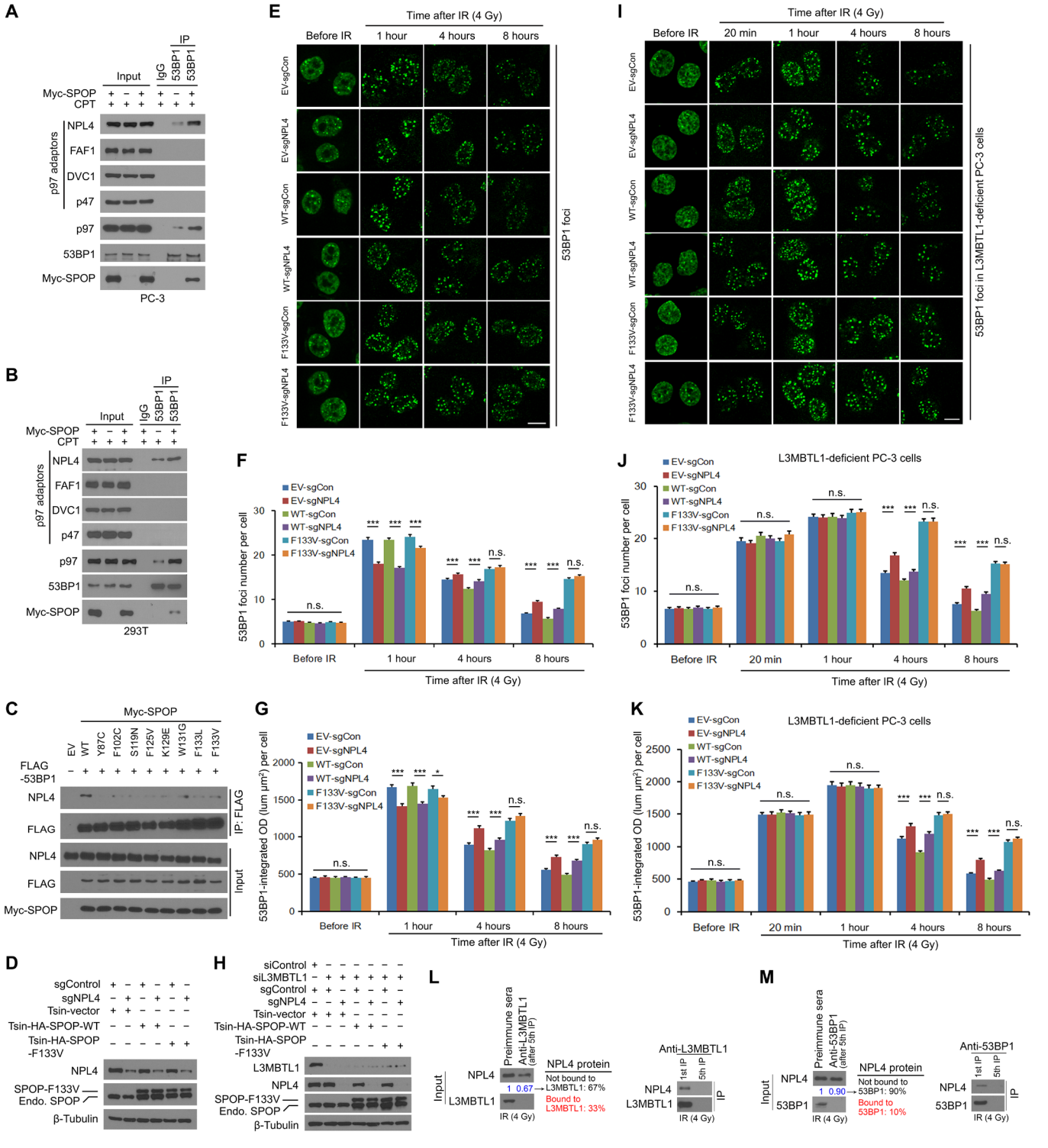

Fig. 5. SPOP regulates 53BP1 interaction with the p97-NPL4 complex and 53BP1 retention at DSB sites. (**A** and **B**) PC-3 (A) and 293T (B) cells transfected or not with Myc-SPOP were treated with 1 μM CPT for 3 hours and harvested for co-IP and WB. (**C**) Co-IP and WB of 293T cells transfected with indicated plasmids and treated with 1 μM CPT for 3 hours. (**D** to **G**) sgControl or sgNPL4 stable PC-3 cells were infected with lentivirus expressing EV, SPOP WT, or mutant F133V followed by WB (D) and IFC (E). The average 53BP1 foci number (F) and foci density (G) in each cell were quantified. Scale bar, 10 μM. Data are presented as means ± SEM of more than 300 cells from three biological replicates. **P* < 0.05 and ****P* < 0.001. (**H** to **K**) L3MBTL1 was depleted by a pool of siRNAs in sgControl or sgNPL4 stable PC-3 cells infected with lentivirus expressing EV and SPOP WT or mutant F133V. Cells were subjected to WB (H) and IFC (I). The average 53BP1 foci number (J) and foci density (K) in each cell were quantified, respectively. Scale bar, 10 μM. Data are presented same as aforementioned. (**L** and **M**) Lysate of PC-3 cells treated with IR (4 Gy for 1 hour) was immunodepleted with preimmune sera or antibodies for L3MBTL1 (L) or 53BP1 (M) five times followed by WB.

cells expressing SPOP WT (Fig. 5, D to G). These data suggest that NPL4 and SPOP act in the same pathway in regulating 53BP1 DSB site retention.

Combined with previous data (*15*), our work suggests that NPL4 facilitates 53BP1 recruitment indirectly through L3MBTL1 extraction and shortens 53BP1 retention time directly by contributing to 53BP1 removal from DSB sites. Consistent with this hypothesis, we observed that in NPL4-deficient cells the numbers of 53BP1 IRIF were comparable at both short and long time points after IR (Fig. 5, D to G). We further tested this hypothesis in L3MBTL1-depleted cells. We knocked down endogenous L3MBTL1 in PC-3 cells using two independent gene-specific small interfering RNAs (siRNAs). As expected, L3MBTL1 knockdown increased 53BP1 IRIF formation specifically at 20 min but not at longer time points (1, 4, and 8 hours) after IR (fig. S4, F to I). Depletion of NPL4 no longer affected 53BP1 recruitment to DSB sites at earlier time points (20 min and 1 hour) but was still able to prolong 53BP1 retention at DSB sites in L3MBTL1-deficient PC-3 cells at 4 to 8 hours after IR, and a similar effect was observed for SPOP F133V mutant but not SPOP WT (Fig. 5, H to K). In agreement with the time point–dependent differential influence of NPL4 on chromatin occupancy of L3MBTL1 and 53BP1, immunodepletion showed that approximately 33% of NPL4 bound to L3MBTL1, but much less (approximately 10%) NPL4 bound to 53BP1 at the early time point (1 hour) of IR (Fig. 5, L and M). Together, our data suggest that SPOP regulates 53BP1 retention at DSB sites by promoting 53BP1 interaction with the VCP/p97 cofactor NPL4.

Prostate cancer–derived SPOP mutants impair DSB end resection and promote chromosomal instability

Consistent with the prolonged retention of 53BP1 at DSB sites in SPOP-mutated cells, expression of SPOP mutants F102C and F133V significantly increased the number of IRIF for SHLD2, a component of the shieldin complex (Fig. 6, A to C) (*11*–*13*). In contrast, the numbers of RPA2, BRCA1, 5-bromo-2′-deoxyuridine (BrdU), and RAD51 IRIF were markedly reduced in SPOP-mutated cells (Fig. 6, D to I, and fig. S5, A to F), suggesting that SPOP mutations inhibit DSB end resection by increasing the DSB site occupancy of 53BP1 and associated factors like the shieldin complex.

In a large cohort of patients with prostate cancer (*36*), mutations in the *SPOP* gene and in other HR pathway genes, such as in *BRCA1*, were mutually exclusive (fig. S5G), which is consistent with our data showing that SPOP is an HR-promoting factor. Analysis of another whole-genome sequencing dataset that we generated from patients with prostate cancer (*47*) showed that tumors with SPOP mutations displayed higher overall copy number alteration (CNA) burden and nonsynonymous single-nucleotide variations than WT SPOP tumors (Fig. 6J). Notably, SPOP mutations correlated with intrachromosomal structural variations (e.g., deletions, inversions, and tandem duplications) but not with interchromosomal structure variations such as balanced interchromosomal rearrangements (Fig. 6K). Similar results were obtained in the large The Cancer Genome Atlas cohort of patients with prostate cancer (fig. S5, H and I). In agreement with these data from patients, CPT treatment of SPOP F133V-expressing benign prostatic epithelial BPH1 cells led to a marked increase in the number of intrachromosomal breaks per cell, which was largely reversed by 53BP1 co-KO (Fig. 6, L and M, and fig. S5, J and K). Therefore, prostate cancer–associated SPOP mutations impair DSB end resection and promote chromosomal instability.

DISCUSSION

A lot is understood about the role of 53BP1 in DNA repair pathway selection—NHEJ versus HR before 53BP1 chromatin recruitment (fig. S6)—through shieldin complex–dependent antagonization of DNA end resection and inhibition of HR (*8*, *11*–*13*, *31*). The mechanisms underlying posttranslational modification–mediated recruitment of 53BP1 to DSB sites are also well understood (*6*, *7*). Notably, 53BP1 is excluded from DSB sites during the G_1-S transition of the cell cycle, while BRCA1 recruitment is elevated (*5*), implying a temporal NHEJ-to-HR switch after chromatin engagement of 53BP1. H4K20 methylation level and status affect 53BP1 binding and direct the choice of repair pathway (*21*, *22*). However, the molecular mechanism underlying this transition from NHEJ to HR had not been fully elucidated. In the present study, we demonstrate that SPOP interacts with 53BP1 at the endogenous level. We further show that SPOP-53BP1 interaction is enhanced in response to DNA damage by ATM-dependent phosphorylation of SPOP that creates a new binding interface with 53BP1. Our data also reveal that SPOP binds to 53BP1 primarily in S phase of the cell cycle and that their interaction promotes K29-linked polyubiquitination of 53BP1. Modified 53BP1 interacts with the ubiquitin-recognizing protein NPL4 that leads to 53BP1 extraction from DSB sites by the VCP/p97-NPL4 segregase complex, resulting in the selection of HR over NHEJ after chromatin engagement of 53BP1 (i.e., postcommitment choice of HR, a less error-prone repair pathway than NHEJ) (fig. S7). Given its nondegradable nature, whether K29-linked polyubiquitinated 53BP1 can be recycled warrants further investigation. Thus, our findings provide a mechanistic explanation as to how SPOP functions as a pro-HR factor that likely fosters genomic stability by minimizing the transmission of DNA lesions from parental to daughter cells during DNA replication. We show that cancer patient–derived SPOP mutations impair DNA end resection and induce chromosomal instability, strongly suggesting that genomic instability in SPOP-mutated cells results from lack of selection of HR due to inefficient exclusion of 53BP1 from DSB sites during S phase (fig. S7).

It has been reported that endogenous SPOP binds ATM and that this interaction is enhanced in response to DNA damage (*29*). It was, however, not known whether SPOP was a phosphorylation substrate of ATM, and if so, which residues were phosphorylated by ATM (*29*). We showed that SPOP is phosphorylated by ATM at S119 in the MATH domain. We discovered that conversion of S119 to aspartate (S119D) altered the conformation of SPOP, resulting in strengthened SPOP-53BP1 interaction and enhanced 53BP1 polyubiquitination to a level comparable to that induced by DNA damage. Similar results were obtained for S119E, another phosphomimetic residue. Furthermore, the S119D or S119E mutations facilitated 53BP1 displacement from DSB sites. Conversely, mutation of S119 to the uncharged asparagine residue (S119N), which often occurs in patients with prostate cancer, promoted 53BP1 retention at DSB sites. To our knowledge, this finding is an unprecedented example where phosphorylation of the substrate-binding domain of an E3 ubiquitin ligase, or a receptor domain in general, regulates its binding with a substrate.

The ubiquitin-selective segregase VCP/p97 is known to associate with monoubiquitin or K29-, K63-, and K48-linked polyubiquitin chains through various cofactors including NPL4, UDF1, and p47 (*48*). Previous studies had shown that VCP/p97-NPL4 promotes initial DSB recruitment of 53BP1 at 1 hour after DNA damage via NPL4-dependent removal of L3MBTL1 that blocks 53BP1 binding

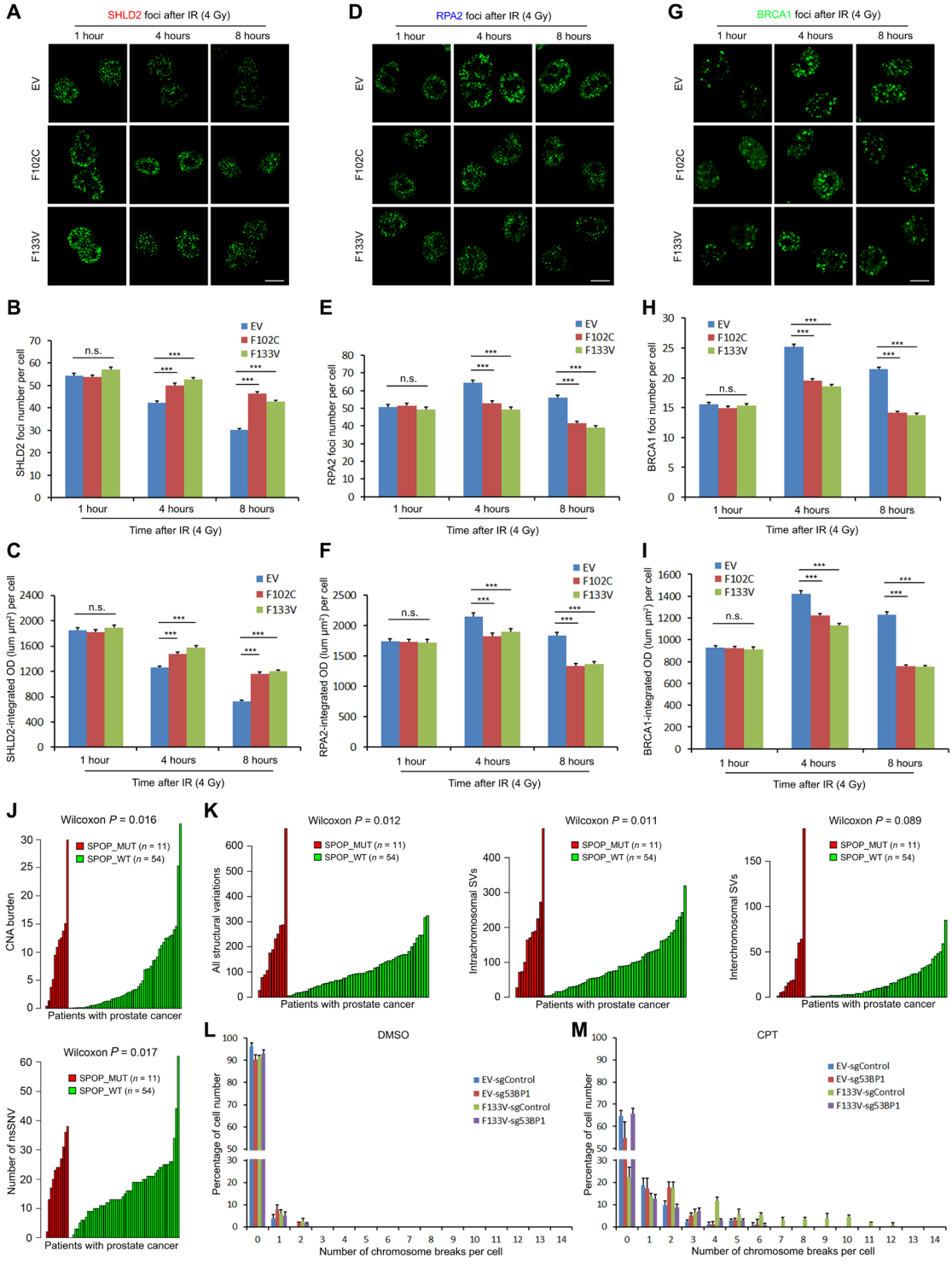

Fig. 6. SPOP mutants impair DNA end resection and chromosomal stability. (**A** to **I**) PC-3 cells infected with EV or lentivirus expressing SPOP mutant F102C or F133V were treated with IR. At each time point after IR, the cells were harvested for IFC with antibodies for SHLD2 (B), RPA2 (D), and BRCA1 (G). The average 53BP1 foci number (B, E, and H) and foci density (C, F, and I) in each cell were quantified. Scale bars, 10 μM. Data are presented as means ± SEM of more than 300 cells from three biological replicates. ***$P < 0.001$. (**J** and **K**) Comparison of CNA burden and nonsynonymous single-nucleotide variation (nsSNV) frequencies per genome between SPOP mutant patients (red bars) and SPOP WT patients (green bars) (J). Comparison of frequencies of structural variations between SPOP mutant patients (red bars) and SPOP WT patients (green bars) (K). *P* values were calculated using two-sided Wilcoxon rank sum test. (**L** and **M**) Control (sgControl) or 53BP1 KO (sg53BP1) BPH1 cells infected with lentivirus expressing EV or SPOP F133V mutant were treated with vehicle (DMSO) (L) or CPT (1 μM) for 24 hours (M). Cells were harvested for karyotyping, and chromosome breaks of more than 300 cells from three biological replicates in each group were counted and quantified.

to chromatin (*49*). In agreement with these findings, we also observed that NPL4 deficiency decreased initial recruitment of 53BP1 at DSB sites. To our surprise, decreased expression of NPL4 paradoxically increased 53BP1 occupancy at DSB sites during the repair stage of DNA damage, implying that NPL4 plays a dual role in regulating both 53BP1 initial recruitment and retention at DSB sites. In NPL4-deficient cells, the numbers of 53BP1 IRIF were comparable at both short and long time points after IR. We further showed that NPL4 knockdown increased 53BP1 retention but did not decrease 53BP1 initial recruitment at DSB sites in L3MBTL1-depleted cells. Furthermore, we uncovered that NPL4 preferentially binds L3MBTL1 over 53BP1 at the acute phase of DNA damage, suggesting that less amount of NPL4 is available for 53BP1 binding during the initial stage of DNA repair. In contrast, more NPL4 is available for 53BP1 binding and eviction at the late stage of DNA repair when L3MBTL1 has been removed. On the basis of our findings, we envision a model where SPOP promotes K29-linked polyubiquitination of 53BP1, which triggers 53BP1 interaction with NPL4 and subsequent eviction of 53BP1 from DSB sites by the VCP/p97-NPL4 complex at the late stage of DNA repair when more NPL4 proteins are available (fig. S7). Our model is also consistent with reports that the zinc finger motif (NZF) in NPL4 and other related proteins is a ubiquitin-binding domain that specifically recognizes K29- and K33-linked ubiquitin chains (*50*).

In summary, our work reveals a hitherto unrecognized role of SPOP in mediating postcommitment choice of the less error-prone DNA repair route by favoring HR through induction of 53BP1 polyubiquitination and exclusion from DSB sites. We show that SPOP is abundantly expressed and has the highest-level interaction with 53BP1 during S phase, which correlates with increased K29-linked polyubiquitination and extraction of 53BP1 at this stage of the cell cycle. Our study introduces SPOP as an HR-promoting factor and provides a molecular mechanism for how 53BP1 is excluded from damaged chromatin in S phase, thereby promoting HR DSB repair. These findings suggest that akin to patients with cancer harboring mutations in other HR pathway genes like *BRCA1* (*51*), those with *SPOP* mutations may also benefit from DNA repair defect–targeted therapies including poly(adenosine diphosphate ribose) polymerase (PARP) inhibition.

MATERIALS AND METHODS

Antibodies and chemicals

The following antibodies were used: SPOP (ab137537, Abcam), SPOP (16750-1-AP, Proteintech), SRC3 (611104, BD Biosciences), BRD4 (13440S, Cell Signaling Technology), DEK (13962S, Cell Signaling Technology), Myc (9E10, Sigma-Aldrich), Myc (sc-40, Santa Cruz Biotechnology), FLAG (M2, Sigma-Aldrich), HA (MM5-101R, Convance), His (sc-8036, Santa Cruz Biotechnology), 53BP1 (MAB3804, Millipore), 53BP1 (ab36823, Abcam), CtIP (sc-271339, Santa Cruz Biotechnology), PTIP (sc-293322, Santa Cruz Biotechnology), Ku80 (2753S, Cell Signaling Technology), BRCA1 (sc-642, Santa Cruz Biotechnology), RPA2 (ab2175, Abcam), RAD51 (ab88572, Abcam), SHLD2 (PA5-39363, Thermo Fisher Scientific), BrdU (ab6326, Abcam), γ-H2AX (9718S, Cell Signaling Technology), γ-H2AX (80312S, Cell Signaling Technology), phospho-RB (9301S, Cell Signaling Technology), phosphor-S/T (612548, BD), β-tubulin (2128S, Cell Signaling Technology), ATM (sc-135663, Santa Cruz Biotechnology), L3MBTL1 (sc-166905, Santa Cruz Biotechnology), NPL4 (sc-365796, Santa Cruz Biotechnology), p47 (sc-365215, Santa Cruz Biotechnology), FAF1 (sc-393965, Santa Cruz Biotechnology), DVC1 (sc-377265, Santa Cruz Biotechnology), p97 (sc-133212, Santa Cruz Biotechnology), cyclin A (sc-271682, Santa Cruz Biotechnology), cyclin B (sc-245, Santa Cruz Biotechnology), cyclin E (ab7959, Abcam), p53 (SC-126, Santa Cruz Biotechnology), and p21 (2946, Cell Signaling Technology). The following chemicals were used: KU-55933 (ATM inhibitor), VE-822 (ATR inhibitor), AZD7762 (CHK1 inhibitor), and GSK1120212 [mitogen-activated protein kinase kinase 1 (MEK1)/MEK2 inhibitor] from Selleckchem; MK-1775 (WEE1 inhibitor) from BioVision; nocodazole from Sigma-Aldrich; CPT from MP Biomedicals LLC; and MG132 (proteasome inhibitor) from EMD Chemicals.

Plasmids and mutagenesis

Expression vectors for SPOP-WT or mutants were described previously (*25*, *28*). The HA-53BP1 construct was obtained from Z. Lou (Mayo Clinic). The green fluorescent protein (GFP)–53BP1 construct was purchased from Addgene (no. 60813). HA-53BP1 mutants were generated using the KOD Plus Mutagenesis Kit (TOYOBO) and following the manufacturer's instructions. LenticrisprV2 plasmid (no. 52961) was purchased from Addgene (USA).

Cell culture, transfection, and lentivirus infection

PC-3, U2OS, and 293T cells were obtained from the American Type Culture Collection. BPH1 cells were provided by S. Hayward. 293T and U2OS cells were maintained in Dulbecco's modified Eagle's medium with 10% fetal bovine serum (FBS), while PC-3 and BPH1 cells were maintained in RPMI medium with 10% FBS. Cells were transiently transfected using Lipofectamine 3000 (for plasmid transfection) or Lipofectamine RNAiMAX (for siRNA transfection) (Thermo Fisher Scientific) according to the manufacturer's instructions. pTsin-HA-SPOP-F133V mutant expression or lenticrisprV2-53BP1 or lenticrisprV2-NPL4 and virus packing constructs were transfected into 293T cells. Virus supernatant was collected 48 hours after transfection. PC-3, U2OS, and BPH1 cells were infected with viral supernatant in the presence of polybrene (8 μg/ml) and were then selected in growth media containing puromycin (1.5 μg/ml). All the cell lines used have been tested and authenticated by karyotyping, and prostate cancer cell lines have also been authenticated by examining SPOP mutation status. Plasmocin (InvivoGen) was added to cell culture media to prevent mycoplasma contamination. Mycoplasma contamination was tested regularly using the LookOut Mycoplasma PCR Detection Kit from Sigma-Aldrich.

RNA interference and sgRNA-mediated gene deletion

Nonspecific control siRNA and siRNAs for CtIP, 53BP1, and L3MBTL1 were purchased from GE Dharmacon. The sequences of siRNA oligos are as follows: si-CtIP#1 5′-GCUAAAACAGGAACGAAUC-3′ and si-CtIP#2 5′-UCCACAACAUAAUCCUAAU-3′; si-53BP1#1 5′-GAGCUGGGAAGUAUAAAUU-3′ and si-53BP1#2 5′-GGACUCCAGUGUUGUCAUU-3′; and si-L3MBTL1#1 5′-GUGGAGGACCAUCGGAUAA-3′ and si-L3MBTL1#2 5′-AAUCAUACCAGAACGUCUA-3′.

siRNA transfection of cells was performed following the manufacturer's instructions. The sequences of sgRNAs are as follows: sgSPOP#1 5′-CACCGCAAGCTTACCCTCTTCTGCG-3′ and sgSPOP#2 5′-CACCGGTCATCAGGGAGAAGCCCGT-3′; sg53BP1#1 5′-CACCGTCCAATCCTGAACAAACAGC-3′ and

sg53BP1#2 5′-CACCGGGGGAGCAGATGGACCCTAC-3′; sgNPL4#1 5′-CACCGGTACTTATACGGACGGTACA-3′ and sgNPL4#2 5′-CACCGTTTAGATAGTCCTCATCGAA-3′; sgBRCA1#1 5′-CACCGTGGTCACACTTTGTGGAGAC-3′ and sgBRCA1#2 5′-CACCGTGCTAGTCTGGAGTTGATCA-3′; sgSpop#1 5′-CACCGTGCCGGTTGGCAGATGAGTT-3′ and sgSpop#2 5′-CACCGTTCGTGCAAGGCAAAGACTG-3′; and sg53bp1#1 5′-CACCGTGACGCGGGTGACGAGTGTA-3′ and sg53bp1#2 5′-CACCGCAGATGTTTATTATGTGGAT-3′.

Coimmunoprecipitation

To immunoprecipitate the ectopically expressed FLAG- or HA-tagged proteins, transfected cells were lysed 24 hours after transfection in BC100 buffer. The whole-cell lysates were immunoprecipitated with the monoclonal anti-FLAG antibody-conjugated M2 agarose beads (Sigma-Aldrich) or HA primary antibody plus protein A/G beads at 4°C overnight. After three washes with lysis buffer, followed by two washes with BC100 buffer, the bound proteins were eluted using FLAG-Peptide (Sigma-Aldrich) prepared in BC100 for 3 hours at 4°C or boiled in 1× LDS (lithium dodecyl sulfate) sample buffer. The eluted protein sample was resolved by SDS–polyacrylamide gel electrophoresis (PAGE). To immunoprecipitate the endogenous proteins, cells were lysed with 1× cell lysis buffer (Cell Signaling Technology), and the lysate was centrifuged. The supernatant was precleared with protein A/G beads (Sigma-Aldrich) and incubated with indicated antibody and protein A/G beads at 4°C overnight. Beads were washed five times with lysis buffer and resuspended in sample buffer and analyzed by SDS-PAGE.

In vivo ubiquitination assay

For in vivo ubiquitination assay, 293T cells transfected with plasmids for HA-Ub or FLAG-Ub, FLAG-53BP1, or HA-53BP1 and other indicated constructs. Cells were harvested and lysed with lysis buffer [50 mM tris-HCl (pH 7.5), 150 mM NaCl, 1% NP-40, 0.5% sodium deoxycholate, and 1× protease inhibitor cocktail]. The lysate was subjected to co-IP using anti-FLAG–conjugated agarose beads or HA primary antibody plus protein A/G beads as described in co-IP assay. For analysis of chromatin-bound ubiquitinated 53BP1, cells were lysed using a subcellular protein fractionation kit purchased from Thermo Fisher Scientific. Cell lysates were subjected to IP and Western blot analysis.

Western blot

Cell lysates or immunoprecipitant was subjected to SDS-PAGE, and proteins were transferred to nitrocellulose membranes (GE Healthcare Sciences). The membranes were blocked in tris-buffered saline (TBS; pH 7.4) containing 5% nonfat milk and 0.1% Tween 20, washed twice in TBS containing 0.1% Tween 20, and incubated with primary antibody overnight at 4°C, followed by secondary antibody for 1 hour at room temperature. The proteins of interest were visualized using an enhanced chemiluminescence system (Thermo Fisher). Densitometry analysis of protein bands was performed using the Gel-Pro Analyzer software.

HR and NHEJ reporter assay

Cells were transfected with siControl, siCtiP or si53BP1, Tsin-HA vector, or Tsin-HA-SPOP-F133V separately, and with combinations of HR (pDR-GFP)– or NHEJ (pPEM1-Ad2-EGFP)–reporter constructs and an expression vector for the restriction enzyme I-Sce I. All plasmids used in the GFP-reporter assay were a gift of Z. Lou (Mayo Clinic). U2OS cells integrated with a DR-GFP cassette as reported previously (*39*) were used to analyze chromosomal HR efficiency. The GFP expression induced by the positive control plasmid was used to normalize the electroporation efficiency. Cells were grown for 48 hours and processed for further flow cytometry analysis.

CSR assay

CH12F3-C2 murine B cell line was provided by X. Wu from Mayo Clinic (*38*). Cells were treated with purified anti-murine CD40 Ab (2 mg/ml; BD Biosciences), recombinant murine interleukin-4 (10 ng/ml; R&D Systems), and recombinant human transforming growth factor–β (1 ng/ml; R&D Systems) for 72 hours. Cells were stained with PE (phycoerythrin)-conjugated anti-murine immunoglobulin A (IgA) clone 1144-2 (12-5994-82 from eBioscience) and fluorescein isothiocyanate–conjugated anti-murine IgM (11-5890-82 from eBioscience) using Cytofix/Cytoperm buffer and washed with permeabilization/wash buffer (BD Biosciences) before analyzed by flow cytometry.

Immunofluorescent chemistry and foci quantification

Cells were seeded on 13-mm glass coverslips. The samples were washed once in ice-cold phosphate-buffered saline (PBS) and fixed with 4% formaldehyde in PBS for 15 min at room temperature. The samples were permeabilized in 0.5% Triton in PBS for 15 min before incubation with primary antibodies for 1 to 2 hours depending on the antibody. The samples were subsequently incubated with secondary fluorescence-coupled antibodies for 1 hour. The coverslips were washed at least three times after antibody incubation. Incubations with antibodies were done in 3% bovine serum albumin in PBS-T (0.01% Tween 20 in PBS), and all washes were performed with PBS-T. Samples were stained with 4′,6-diamidino-2-phenylindole at 10 mg/ml for 5 min before being mounted on glass slides and visualized using a fluorescence microscope. Depending on the experiment, DNA damage foci were either counted manually or quantified using the Image-Pro software. For each cell line analyzed with Image-Pro, 10 randomly picked photographs that included more than 200 cells were used to standardize foci counting and integration of optical density. This approach was used to analyze approximately 300 cells for each series of experiments. Cyclin A–positive 53BP1 foci were selected and analyzed using Image-Pro.

Cell synchronization

For synchronization, PC-3 cells were treated with nocodazole (100 ng/ml) for 12 hours and were released into regular medium. At the indicated time points after releasing, cells were harvested for cell cycle profiling, Western blot, and co-IP analyses.

Karyotype analysis

BPH1 cells were treated with 1 μM CPT for 24 hours and colcemid for 45 min before harvest. Cells were washed two times in PBS and then resuspended in 0.075 M KCl at 37°C for 8 min. Cells were fixed with fixative (3:1 methanol:glacial acetic acid) twice, for 15 min each time. Small drops of cell suspension were dropped onto slide surface and stained with Diff-Quik staining for 1 min. About 100 cells with well-spread chromosomes were photographed, analyzed, and counted for breaks.

Protein and peptide preparation and purification

SPOP-MATH (residues 28 to 164) WT and S119D, S119A and S199N mutants and 53BP1 (residues 1606 to 1656) were cloned in a

pET-based expression vector with an N-terminal His_6 tag cleavable by PreScission protease. Two extra residues, Gly and Trp, were included at the C terminus of 53BP1 for protein quantification by ultraviolet light absorbance. The five proteins were expressed in BL21 (DE3) cells grown in appropriate media (LB media, ^{15}N-enriched M9 media, or ^{13}C-,^{15}N-enriched 9 media) at 37°C to OD_{600} (optical density at 600 nm) 0.6 and then at 15°C for 16 hours following induction with isopropyl-β-D-thiogalactoside (final concentration, 0.5 mM). The harvested cells were lysed with a microfluidizer (Avestin Emulsiflex C5). The proteins were purified by Ni^{2+}–nitrilotriacetic acid agarose chelation chromatography (QIAGEN) and incubated with PreScission protease overnight at 4°C to cleave the His_6 tag. The proteins were further purified by size exclusion chromatography using a HiLoad 16/60 Superdex 75 column (GE Healthcare). The 53BP1 SBM synthetic peptide (residues 1636 to 1650) was purified by reversed-phase chromatography using a Jupiter 5-μm C18 300 preparative column (Phenomenex).

NMR spectroscopy

All NMR spectra were recorded using a 700-MHz Bruker Avance III spectrometer equipped with a cryogenically cooled triple-resonance probe. NMR samples were prepared in 10 mM Na_2HPO_4/1.76 mM KH_2PO_4 (pH 6.0), 50 mM NaCl, 2.7 mM KCl, and 5 mM dithiothreitol (DTT). A 0.9 mM ^{13}C-, ^{15}N-labeled $53BP1^{1606–1656}$ sample was used for the backbone resonance assignments. Assignments were obtained from a series of standard NMR experiments including 2D ^{1}H-^{15}N HSQC, 3D HBCACB, 3D CBCA(CO)NH, 3D HNCO, 3D HN(CA)CO, 3D HBHA(CO)NH, and 3D ^{15}N-NOESY. For NMR-based titration assays, ^{15}N-labeled $53BP1^{1606–1656}$ and ^{15}N-labeled SPOP MATH were at a concentration of 0.2 mM. The unlabeled protein stock solutions used for the titrations were at concentrations of 6 mM ($53BP1^{1606–1656}$) and 5.4 mM (SPOP MATH). The titrations of ^{15}N-labeled $53BP1^{1606–1656}$ and ^{15}N-labeled SPOP MATH were done at 4° and 25°C, respectively. The NMR data were processed with NMRpipe (*52*) and analyzed with NMRViewJ (*53*).

X-ray crystallography

Crystals were grown by the hanging drop method, mixing 2 μl of the protein sample in 20 mM tris-HCl (pH 7.6), 150 mM NaCl, 5 mM DTT, and 2 μl of the reservoir solution for the drop. The reservoir solution was 0.5 ml. Crystallization plates were kept at 22°C. Crystals of apo SPOP MATH were obtained using protein sample (24 mg/ml) and reservoir solution 1 [0.1 M sodium citrate tribasic dihydrate (pH 5.6), 0.2 M $(NH_4)_2SO_4$, and 1 M Li_2SO_4]. Crystals of SPOP MATH-53BP1 peptide complex were obtained using a protein sample (24 mg/ml) with a 1:5 protein:peptide molar ratio, and reservoir solution 1. For the SPOP MATH and SPOP MATH-53BP1 peptide structures, we used a D140G mutation in SPOP that facilitates crystallization (*32*). Crystals of SPOP MATH S119D-53BP1 peptide complex were obtained using protein solution (20 mg/ml) containing peptide with a 1:5 protein:peptide molar ratio, and reservoir solution 2 [2 M $(NH_4)_2SO_4$]. Crystals of SPOP MATH S119A were obtained using protein solution (20 mg/ml) and reservoir solution 3 [0.2 M $(NH4)_2SO_4$, 0.1 M bis-tris (pH 6.5), and 25% (w/v) polyethylene glycol, molecular weight 3350]. Crystals of SPOP MATH S119A were cryoprotected with 30% (v/v) glycerol, while all other crystals were cryoprotected with 25% (w/v) xylitol, prepared from the respective reservoir solutions, and quick-frozen with liquid nitrogen. X-ray diffraction data were collected at the19-BM or 19-ID beamline of the Advanced Photon Source, Argonne National Laboratory, IL, using one crystal for each sample. For apo and 53BP1 peptide-bound SPOP crystals, the corresponding space groups were C 1 2 1 and C 2 2 21, with one molecule or complex in the asymmetric unit. Crystals of 53BP1 peptide-bound SPOP MATH S119D were in the P 41 21 2 space group, with two complexes in the asymmetric unit. Crystals of SPOP MATH S119A were in the P61 2 2 space group with one molecule in the asymmetric unit. Diffraction data were indexed, integrated, and scaled with HKL2000. Initial phases for the SPOP-53BP1 peptide complex were obtained by molecular replacement using the atomic coordinates in Protein Data Bank entry 3HQM as a search model in PHENIX (*54*). Using the final coordinates of SPOP-53BP1 above as search model for molecular replacement, the initial phases of SPOP S119D-53BP1 peptide complex was obtained. Using the same SPOP-53BP1 coordinates above but without the peptide chain as search model for molecular replacement, the initial phases of apo SPOP and S119A were obtained. Models were built and refined iteratively in COOT (*55*) and in PHENIX. Statistics of the final structures are shown in table S1. Molecular representations were generated with PyMOL (The PyMOL Molecular Graphics System, versions 1.8.0.6 and 2.1 Schrödinger LLC).

Isothermal titration calorimetry

The titrations were performed using a MicroCal iTC200 instrument (Malvern) with the SPOP MATH domain proteins (WT and mutants) and 53BP1 peptide dissolved in 25 mM tris-HCl (pH 7.5), 100 mM NaCl. Each ITC run was performed at 10°C with SPOP MATH in the reaction cell at a concentration of 100 μM and the 53BP1 peptide in the injection syringe at concentrations of 2 to 4 mM. For each run, there were 19 injections with a volume of 2 μl and a duration of 4 s. Injection spacing was 3 min and the stirring speed rate was 750 rpm. Data were analyzed using a one-site model with Levenberg-Marquardt nonlinear regression programmed in the Origin 7.0 software (OriginLab).

Differential scanning fluorimetry with SYPRO Orange

The differential scanning fluorimetry measurements were carried out using a Bio-Rad CFX96 Touch Real-Time PCR system in 96-well plates and a reaction volume of 50 μl. The SPOP MATH protein constructs (WT, S119A, and S119D) were at a concentration of 30 μM in 50 mM sodium phosphate buffer (pH 7.5), 300 mM NaCl. The SYPRO Orange dye (Sigma-Aldrich) was used at a concentration of 10×. The temperature was continuously increased from 25° to 95°C at 1°C/min. The fluorescence intensity was measured every minute. Three replicate measurements were performed.

Analysis of copy number variations, somatic mutations, and structure variations in prostate cancer patient specimens

Whole-genome high-throughput sequencing data from 65 paired tumors and matched adjacent benign tissues from primary prostate cancer patient samples reported previously (*47*) were analyzed as described for copy number variations (CNAs), somatic mutations, and structure variations.

Statistical analysis

All data are shown as mean values ± SD or mean values ± SEM for experiments performed with at least three replicates. The difference between two groups was analyzed using paired Student's *t* test

unless otherwise specified. A P value less than 0.05 is considered statistically significant.

SUPPLEMENTARY MATERIALS

Supplementary material for this article is available at http://advances.sciencemag.org/cgi/content/full/7/25/eabd9208/DC1

View/request a protocol for this paper from *Bio-protocol*.

REFERENCES AND NOTES

1. N. Hustedt, D. Durocher, The control of DNA repair by the cell cycle. *Nat. Cell Biol.* **19**, 1–9 (2016).
2. B. Wang, S. Matsuoka, P. B. Carpenter, S. J. Elledge, 53BP1, a mediator of the DNA damage checkpoint. *Science* **298**, 1435–1438 (2002).
3. N. Dimitrova, Y.-C. Chen, D. L. Spector, T. de Lange, 53BP1 promotes non-homologous end joining of telomeres by increasing chromatin mobility. *Nature* **456**, 524–528 (2008).
4. S. F. Bunting, E. Callén, N. Wong, H. T. Chen, F. Polato, A. Gunn, A. Bothmer, N. Feldhahn, O. Fernandez-Capetillo, L. Cao, X. Xu, C. X. Deng, T. Finkel, M. Nussenzweig, J. M. Stark, A. Nussenzweig, 53BP1 inhibits homologous recombination in Brca1-deficient cells by blocking resection of DNA breaks. *Cell* **141**, 243–254 (2010).
5. J. R. Chapman, A. J. Sossick, S. J. Boulton, S. P. Jackson, BRCA1-associated exclusion of 53BP1 from DNA damage sites underlies temporal control of DNA repair. *J. Cell Sci.* **125**, 3529–3534 (2012).
6. A. Fradet-Turcotte, M. D. Canny, C. Escribano-Díaz, A. Orthwein, C. C. Y. Leung, H. Huang, M. C. Landry, J. Kitevski-LeBlanc, S. M. Noordermeer, F. Sicheri, D. Durocher, 53BP1 is a reader of the DNA-damage-induced H2A Lys 15 ubiquitin mark. *Nature* **499**, 50–54 (2013).
7. M. V. Botuyan, J. Lee, I. M. Ward, J. E. Kim, J. R. Thompson, J. Chen, G. Mer, Structural basis for the methylation state-specific recognition of histone H4-K20 by 53BP1 and Crb2 in DNA repair. *Cell* **127**, 1361–1373 (2006).
8. M. Zimmermann, F. Lottersberger, S. B. Buonomo, A. Sfeir, T. de Lange, 53BP1 regulates DSB repair using Rif1 to control 5′ end resection. *Science* **339**, 700–704 (2013).
9. I. M. Munoz, P. A. Jowsey, R. Toth, J. Rouse, Phospho-epitope binding by the BRCT domains of hPTIP controls multiple aspects of the cellular response to DNA damage. *Nucleic Acids Res.* **35**, 5312–5322 (2007).
10. J. A. Schmid, M. Berti, F. Walser, M. C. Raso, F. Schmid, J. Krietsch, H. Stoy, K. Zwicky, S. Ursich, R. Freire, M. Lopes, L. Penengo, Histone ubiquitination by the DNA damage response is required for efficient DNA replication in unperturbed S phase. *Mol. Cell* **71**, 897–910.e8 (2018).
11. Z. Mirman, F. Lottersberger, H. Takai, T. Kibe, Y. Gong, K. Takai, A. Bianchi, M. Zimmermann, D. Durocher, T. de Lange, 53BP1–RIF1–shieldin counteracts DSB resection through CST- and Polα-dependent fill-in. *Nature* **560**, 112–116 (2018).
12. S. M. Noordermeer, S. Adam, D. Setiaputra, M. Barazas, S. J. Pettitt, A. K. Ling, M. Olivieri, A. Álvarez-Quilón, N. Moatti, M. Zimmermann, S. Annunziato, D. B. Krastev, F. Song, I. Brandsma, J. Frankum, R. Brough, A. Sherker, S. Landry, R. K. Szilard, M. M. Munro, A. McEwan, T. Goullet de Rugy, Z. Y. Lin, T. Hart, J. Moffat, A. C. Gingras, A. Martin, H. van Attikum, J. Jonkers, C. J. Lord, S. Rottenberg, D. Durocher, The shieldin complex mediates 53BP1-dependent DNA repair. *Nature* **560**, 117–121 (2018).
13. H. Ghezraoui, C. Oliveira, J. R. Becker, K. Bilham, D. Moralli, C. Anzilotti, R. Fischer, M. Deobagkar-Lele, M. Sanchiz-Calvo, E. Fueyo-Marcos, S. Bonham, B. M. Kessler, S. Rottenberg, R. J. Cornall, C. M. Green, J. R. Chapman, 53BP1 cooperation with the REV7-shieldin complex underpins DNA structure-specific NHEJ. *Nature* **560**, 122–127 (2018).
14. J. Lee, J. R. Thompson, M. V. Botuyan, G. Mer, Distinct binding modes specify the recognition of methylated histones H3K4 and H4K20 by JMJD2A-tudor. *Nat. Struct. Mol. Biol.* **15**, 109–111 (2008).
15. K. Acs, M. S. Luijsterburg, L. Ackermann, F. A. Salomons, T. Hoppe, N. P. Dantuma, The AAA-ATPase VCP/p97 promotes 53BP1 recruitment by removing L3MBTL1 from DNA double-strand breaks. *Nat. Struct. Mol. Biol.* **18**, 1345–1350 (2011).
16. F. A. Mallette, F. Mattiroli, G. Cui, L. C. Young, M. J. Hendzel, G. Mer, T. K. Sixma, S. Richard, RNF8- and RNF168-dependent degradation of KDM4A/JMJD2A triggers 53BP1 recruitment to DNA damage sites. *EMBO J.* **31**, 1865–1878 (2012).
17. K. Y. Hsiao, C. A. Mizzen, Histone H4 deacetylation facilitates 53BP1 DNA damage signaling and double-strand break repair. *J. Mol. Cell Biol.* **5**, 157–165 (2013).
18. K. Jacquet, A. Fradet-Turcotte, N. Avvakumov, J.-P. Lambert, C. Roques, R. K. Pandita, E. Paquet, P. Herst, A. C. Gingras, T. K. Pandita, G. Legube, Y. Doyon, D. Durocher, J. Côté, The TIP60 complex regulates bivalent chromatin recognition by 53BP1 through direct H4K20me binding and H2AK15 acetylation. *Mol. Cell* **62**, 409–421 (2016).
19. P. Drané, M.-E. Brault, G. Cui, K. Meghani, S. Chaubey, A. Detappe, N. Parnandi, Y. He, X.-F. Zheng, M. V. Botuyan, A. Kalousi, W. T. Yewdell, C. Münch, J. W. Harper, J. Chaudhuri, E. Soutoglou, G. Mer, D. Chowdhury, TIRR regulates 53BP1 by masking its histone methyl-lysine binding function. *Nature* **543**, 211–216 (2017).
20. M. V. Botuyan, G. Cui, P. Drané, C. Oliveira, A. Detappe, M. E. Brault, N. Parnandi, S. Chaubey, J. R. Thompson, B. Bragantini, D. Zhao, J. R. Chapman, D. Chowdhury, G. Mer, Mechanism of 53BP1 activity regulation by RNA-binding TIRR and a designer protein. *Nat. Struct. Mol. Biol.* **25**, 591–600 (2018).
21. S. Pellegrino, J. Michelena, F. Teloni, R. Imhof, M. Altmeyer, Replication-coupled dilution of H4K20me2 guides 53BP1 to pre-replicative chromatin. *Cell Rep.* **19**, 1819–1831 (2017).
22. K. Nakamura, G. Saredi, J. R. Becker, B. M. Foster, N. V. Nguyen, T. E. Beyer, L. C. Cesa, P. A. Faull, S. Lukauskas, T. Frimurer, J. R. Chapman, T. Bartke, A. Groth, H4K20me0 recognition by BRCA1-BARD1 directs homologous recombination to sister chromatids. *Nat. Cell Biol.* **21**, 311–318 (2019).
23. C. E. Barbieri, S. C. Baca, M. S. Lawrence, F. Demichelis, M. Blattner, J. P. Theurillat, T. A. White, P. Stojanov, E. van Allen, N. Stransky, E. Nickerson, S.-S. Chae, G. Boysen, D. Auclair, R. C. Onofrio, K. Park, N. Kitabayashi, T. Y. MacDonald, K. Sheikh, T. Vuong, C. Guiducci, K. Cibulskis, A. Sivachenko, S. L. Carter, G. Saksena, D. Voet, W. M. Hussain, A. H. Ramos, W. Winckler, M. C. Redman, K. Ardlie, A. K. Tewari, J. M. Mosquera, N. Rupp, P. J. Wild, H. Moch, C. Morrissey, P. S. Nelson, P. W. Kantoff, S. B. Gabriel, T. R. Golub, M. Meyerson, E. S. Lander, G. Getz, M. A. Rubin, L. A. Garraway, Exome sequencing identifies recurrent SPOP, FOXA1 and MED12 mutations in prostate cancer. *Nat. Genet.* **44**, 685–689 (2012).
24. Cancer Genome Atlas Research Network, The molecular taxonomy of primary prostate cancer. *Cell* **163**, 1011–1025 (2015).
25. J. An, C. Wang, Y. Deng, L. Yu, H. Huang, Destruction of full-length androgen receptor by wild-type SPOP, but not prostate-cancer-associated mutants. *Cell Rep.* **6**, 657–669 (2014).
26. C. Geng, B. He, L. Xu, C. E. Barbieri, V. K. Eedunuri, S. A. Chew, M. Zimmermann, R. Bond, J. Shou, C. Li, M. Blattner, D. M. Lonard, F. Demichelis, C. Coarfa, M. A. Rubin, P. Zhou, B. W. O'Malley, N. Mitsiades, Prostate cancer-associated mutations in speckle-type POZ protein (SPOP) regulate steroid receptor coactivator 3 protein turnover. *Proc. Natl. Acad. Sci. U.S.A.* **110**, 6997–7002 (2013).
27. J.-P. Theurillat, N. D. Udeshi, W. J. Errington, T. Svinkina, S. C. Baca, M. Pop, P. J. Wild, M. Blattner, A. C. Groner, M. A. Rubin, H. Moch, G. G. Prive, S. A. Carr, L. A. Garraway, Ubiquitylome analysis identifies dysregulation of effector substrates in SPOP-mutant prostate cancer. *Science* **346**, 85–89 (2014).
28. P. Zhang, D. Wang, Y. Zhao, S. Ren, K. Gao, Z. Ye, S. Wang, C. W. Pan, Y. Zhu, Y. Yan, Y. Yang, D. Wu, Y. He, J. Zhang, D. Lu, X. Liu, L. Yu, S. Zhao, Y. Li, D. Lin, Y. Wang, L. Wang, Y. Chen, Y. Sun, C. Wang, H. Huang, Intrinsic BET inhibitor resistance in SPOP-mutated prostate cancer is mediated by BET protein stabilization and AKT-mTORC1 activation. *Nat. Med.* **23**, 1055–1062 (2017).
29. D. Zhang, H. Wang, M. Sun, J. Yang, W. Zhang, S. Han, B. Xu, Speckle-type POZ protein, SPOP, is involved in the DNA damage response. *Carcinogenesis* **35**, 1691–1697 (2014).
30. G. Boysen, C. E. Barbieri, D. Prandi, M. Blattner, S.-S. Chae, A. Dahija, S. Nataraj, D. Huang, C. Marotz, L. Xu, J. Huang, P. Lecca, S. Chhangawala, D. Liu, P. Zhou, A. Sboner, J. S. de Bono, F. Demichelis, Y. Houvras, M. A. Rubin, SPOP mutation leads to genomic instability in prostate cancer. *eLife* **4**, e09207 (2015).
31. K. Hjorth-Jensen, A. Maya-Mendoza, N. Dalgaard, J. O. Sigurðsson, J. Bartek, D. Iglesias-Gato, J. V. Olsen, A. Flores-Morales, SPOP promotes transcriptional expression of DNA repair and replication factors to prevent replication stress and genomic instability. *Nucleic Acids Res.* **46**, 9484–9495 (2018).
32. M. Zhuang, M. F. Calabrese, J. Liu, M. B. Waddell, A. Nourse, M. Hammel, D. J. Miller, H. Walden, D. M. Duda, S. N. Seyedin, T. Hoggard, J. W. Harper, K. P. White, B. A. Schulman, Structures of SPOP-substrate complexes: Insights into molecular architectures of BTB-Cul3 ubiquitin ligases. *Mol. Cell* **36**, 39–50 (2009).
33. N. E. Hafsa, D. Arndt, D. S. Wishart, CSI 3.0: A web server for identifying secondary and super-secondary structure in proteins using NMR chemical shifts. *Nucleic Acids Res.* **43**, W370–W377 (2015).
34. W. K. Pierce, C. R. Grace, J. Lee, A. Nourse, M. R. Marzahn, E. R. Watson, A. A. High, J. Peng, B. A. Schulman, T. Mittag, Multiple weak linear motifs enhance recruitment and processivity in SPOP-mediated substrate ubiquitination. *J. Mol. Biol.* **428**, 1256–1271 (2016).
35. M. S. Ostertag, A. C. Messias, M. Sattler, G. M. Popowicz, The structure of the SPOP-Pdx1 interface reveals insights into the phosphorylation-dependent binding regulation. *Structure* **27**, 327–334.e3 (2019).
36. J. Armenia, S. A. M. Wankowicz, D. Liu, J. Gao, R. Kundra, E. Reznik, W. K. Chatila, D. Chakravarty, G. C. Han, I. Coleman, B. Montgomery, C. Pritchard, C. Morrissey, C. E. Barbieri, H. Beltran, A. Sboner, Z. Zafeiriou, S. Miranda, C. M. Bielski, A. V. Penson, C. Tolonen, F. W. Huang, D. Robinson, Y. M. Wu, R. Lonigro, L. A. Garraway, F. Demichelis, P. W. Kantoff, M.-E. Taplin, W. Abida, B. S. Taylor, H. I. Scher, P. S. Nelson, J. S. de Bono, M. A. Rubin, C. L. Sawyers, A. M. Chinnaiyan; PCF/SUC International Prostate Cancer Dream Team, N. Schultz, E. M. Van Allen, The long tail of oncogenic drivers in prostate cancer. *Nat. Genet.* **50**, 645–651 (2018).
37. M. Blattner, D. Liu, B. D. Robinson, D. Huang, A. Poliakov, D. Gao, S. Nataraj, L. D. Deonarine, M. A. Augello, V. Sailer, L. Ponnala, M. Ittmann, A. M. Chinnaiyan,

A. Sboner, Y. Chen, M. A. Rubin, C. E. Barbieri, SPOP mutation drives prostate tumorigenesis in vivo through coordinate regulation of PI3K/mTOR and AR signaling. *Cancer Cell* **31**, 436–451 (2017).
38. H. Pei, X. Wu, T. Liu, K. Yu, D. F. Jelinek, Z. Lou, The histone methyltransferase MMSET regulates class switch recombination. *J. Immunol.* **190**, 756–763 (2013).
39. A. Gunn, J. M. Stark, I-SceI-based assays to examine distinct repair outcomes of mammalian chromosomal double strand breaks. *Methods Mol. Biol.* **920**, 379–391 (2012).
40. R. Cuella-Martin, C. Oliveira, H. E. Lockstone, S. Snellenberg, N. Grolmusova, J. R. Chapman, 53BP1 integrates DNA repair and p53-dependent cell fate decisions via distinct mechanisms. *Mol. Cell* **64**, 51–64 (2016).
41. N. Singh, H. Basnet, T. D. Wiltshire, D. H. Mohammad, J. R. Thompson, A. Héroux, M. V. Botuyan, M. B. Yaffe, F. J. Couch, M. G. Rosenfeld, G. Mer, Dual recognition of phosphoserine and phosphotyrosine in histone variant H2A.X by DNA damage response protein MCPH1. *Proc. Natl. Acad. Sci. U.S.A.* **109**, 14381–14386 (2012).
42. M. S. Ostertag, W. Hutwelker, O. Plettenburg, M. Sattler, G. M. Popowicz, Structural insights into BET client recognition of endometrial and prostate cancer-associated SPOP mutants. *J. Mol. Biol.* **431**, 2213–2221 (2019).
43. J. J. Bouchard, J. H. Otero, D. C. Scott, E. Szulc, E. W. Martin, N. Sabri, D. Granata, M. R. Marzahn, K. Lindorff-Larsen, X. Salvatella, B. A. Schulman, T. Mittag, Cancer mutations of the tumor suppressor SPOP disrupt the formation of active, phase-separated compartments. *Mol. Cell* **72**, 19–36.e8 (2018).
44. S. Kilic, A. Lezaja, M. Gatti, E. Bianco, J. Michelena, R. Imhof, M. Altmeyer, Phase separation of 53BP1 determines liquid-like behavior of DNA repair compartments. *EMBO J.* **38**, e101379 (2019).
45. J. Zhang, X. Bu, H. Wang, Y. Zhu, Y. Geng, N. T. Nihira, Y. Tan, Y. Ci, F. Wu, X. Dai, J. Guo, Y.-H. Huang, C. Fan, S. Ren, Y. Sun, G. J. Freeman, P. Sicinski, W. Wei, Cyclin D-CDK4 kinase destabilizes PD-L1 via cullin 3-SPOP to control cancer immune surveillance. *Nature* **553**, 91–95 (2018).
46. I. Torrecilla, J. Oehler, K. Ramadan, The role of ubiquitin-dependent segregase p97 (VCP or Cdc48) in chromatin dynamics after DNA double strand breaks. *Philos. Trans. R. Soc. Lond. B Biol. Sci.* **372**, 20160282 (2017).
47. S. Ren, G.-H. Wei, D. Liu, L. Wang, Y. Hou, S. Zhu, L. Peng, Q. Zhang, Y. Cheng, H. Su, X. Zhou, J. Zhang, F. Li, H. Zheng, Z. Zhao, C. Yin, Z. He, X. Gao, H. E. Zhau, C.-Y. Chu, J. B. Wu, C. Collins, S. V. Volik, R. Bell, J. Huang, K. Wu, D. Xu, D. Ye, Y. Yu, L. Zhu, M. Qiao, H.-M. Lee, Y. Yang, Y. Zhu, X. Shi, R. Chen, Y. Wang, W. Xu, Y. Cheng, C. Xu, X. Gao, T. Zhou, B. Yang, J. Hou, L. Liu, Z. Zhang, Y. Zhu, C. Qin, P. Shao, J. Pang, L. W. K. Chung, J. Xu, C.-L. Wu, W. Zhong, X. Xu, Y. Li, X. Zhang, J. Wang, H. Yang, J. Wang, H. Huang, Y. Sun, Whole-genome and transcriptome sequencing of prostate cancer identify new genetic alterations driving disease progression. *Eur. Urol.* **73**, 322–339 (2017).
48. H. Meyer, C. C. Weihl, The VCP/p97 system at a glance: Connecting cellular function to disease pathogenesis. *J. Cell Sci.* **127**, 3877–3883 (2014).
49. M. Meerang, D. Ritz, S. Paliwal, Z. Garajova, M. Bosshard, N. Mailand, P. Janscak, U. Hübscher, H. Meyer, K. Ramadan, The ubiquitin-selective segregase VCP/p97 orchestrates the response to DNA double-strand breaks. *Nat. Cell Biol.* **13**, 1376–1382 (2011).
50. M. A. Michel, P. R. Elliott, K. N. Swatek, M. Simicek, J. N. Pruneda, J. L. Wagstaff, S. M. V. Freund, D. Komander, Assembly and specific recognition of k29- and k33-linked polyubiquitin. *Mol. Cell* **58**, 95–109 (2015).
51. J. Mateo, S. Carreira, S. Sandhu, S. Miranda, H. Mossop, R. Perez-Lopez, D. Nava Rodrigues, D. Robinson, A. Omlin, N. Tunariu, G. Boysen, N. Porta, P. Flohr, A. Gillman, I. Figueiredo, C. Paulding, G. Seed, S. Jain, C. Ralph, A. Protheroe, S. Hussain, R. Jones, T. Elliott, U. McGovern, D. Bianchini, J. Goodall, Z. Zafeiriou, C. T. Williamson, R. Ferraldeschi, R. Riisnaes, B. Ebbs, G. Fowler, D. Roda, W. Yuan, Y. M. Wu, X. Cao, R. Brough, H. Pemberton, R. A'Hern, A. Swain, L. P. Kunju, R. Eeles, G. Attard, C. J. Lord, A. Ashworth, M. A. Rubin, K. E. Knudsen, F. Y. Feng, A. M. Chinnaiyan, E. Hall, J. S. de Bono, DNA-repair defects and olaparib in metastatic prostate cancer. *N. Engl. J. Med.* **373**, 1697–1708 (2015).
52. F. Delaglio, S. Grzesiek, G. W. Vuister, G. Zhu, J. Pfeifer, A. Bax, NMRPipe: A multidimensional spectral processing system based on UNIX pipes. *J. Biomol. NMR* **6**, 277–293 (1995).
53. B. A. Johnson, R. A. Blevins, NMR View: A computer program for the visualization and analysis of NMR data. *J. Biomol. NMR* **4**, 603–614 (1994).
54. P. D. Adams, P. V. Afonine, G. Bunkóczi, V. B. Chen, I. W. Davis, N. Echols, J. J. Headd, L. W. Hung, G. J. Kapral, R. W. Grosse-Kunstleve, A. J. McCoy, N. W. Moriarty, R. Oeffner, R. J. Read, D. C. Richardson, J. S. Richardson, T. C. Terwilliger, P. H. Zwart, PHENIX: A comprehensive Python-based system for macromolecular structure solution. *Acta Crystallogr. D Biol. Crystallogr.* **66**, 213–221 (2010).
55. P. Emsley, K. Cowtan, Coot: Model-building tools for molecular graphics. *Acta Crystallogr. D Biol. Crystallogr.* **60**, 2126–2132 (2004).

Acknowledgments: X-ray diffraction data were collected at beamline 19-BM of Argonne National Laboratory, Structural Biology Center at the Advanced Photon Source. Structural Biology Center is operated by UChicago Argonne LLC, for the U.S. Department of Energy, Office of Biological and Environmental Research, under contract DE-AC02-06CH11357. We are very grateful to Y. Kim at the Structural Biology Center for assistance with x-ray data collection. **Funding:** This work was supported, in part, by grants from the National Institutes of Health (CA134514, CA130908, CA193239, and CA203849 to H.H., and CA132878 and GM116829 to G.M.), the Mayo Clinic Foundation (to H.H.), and the National Natural Science Foundation of China (81672544 and 81872099 to D.Y., and 81960502 and 82073083 to D.W.). M.V.B. acknowledges support from the OCRA Liz Tilberis Award. **Author contributions:** H.H. conceived the study. M.V.B., G.C., and G.M. conceived and performed the structural studies. D.W., J.M., Y.Y., D.D., Y.Z., E.W.K., J.P., H.P., and X.W. performed experiments, data collection, and analysis. L.W. performed bioinformatics analysis. H.H., G.M., D.Y., M.A.M., J.M., M.V.B., and D.W. supervised the study and wrote the manuscript. **Competing interests:** The authors declare that they have no competing interests. **Data and materials availability:** All data needed to evaluate the conclusions in the paper are present in the paper and/or the Supplementary Materials. The atomic coordinates for the protein structures presented in this publication are deposited in the Protein Data Bank under accession codes 7LIN, 7LIO, 7LIP, and 7LIQ. Additional data related to this paper may be requested from the authors.

Submitted 21 July 2020
Accepted 4 May 2021
Published 18 June 2021
10.1126/sciadv.abd9208

Citation: D. Wang, J. Ma, M. V. Botuyan, G. Cui, Y. Yan, D. Ding, Y. Zhou, E. W. Krueger, J. Pei, X. Wu, L. Wang, H. Pei, M. A. McNiven, D. Ye, G. Mer, H. Huang, ATM-phosphorylated SPOP contributes to 53BP1 exclusion from chromatin during DNA replication. *Sci. Adv.* **7**, eabd9208 (2021).